A measurement of the surface radioactivity and its time dependence in the SNO+ detector

by

Karl Marie Yazigi

A thesis submitted in partial fulfillment of the requirements for the degree of

Master of Science

Department of Physics
University of Alberta

Abstract

This thesis provides an investigation of various aspects of the major background in the SNO+ experiment and its associated detector.

The initial chapters present an overview of neutrino physics and the SNO+ detector, providing relevant background information.

The impact of light reflection on the detector surface and its influence on event position reconstruction is investigated. A novel methodology is introduced to detect mis-reconstructed events, effectively mitigating the issue. Mis-reconstruction is eliminated within a radius of 5.1m from the detector center and significantly reduced by a factor of 400 within a radius of 5.5m.

The flow patterns of unmixed ^{210}Po within the detector are investigated, and the volume flow rate of this material is estimated to be $\frac{V}{t} = 0.11 \pm 0.019 \, \frac{\text{m}^3}{\text{h}}$. The origin of this material is traced to approximately 10cm from the surface of the detector using the authors mis-reconstruction detection algorithm.

The thesis also focuses on the examination and separation of individual event rates for major backgrounds on the detector surface: ^{210}Po, ^{210}Bi, and ^{14}C. A theoretical simulation of the ^{210}Bi energy spectrum is employed, which is then compared to the observed energy spectrum within the detector. Through analysis, separate event rates for each isotope are determined. Rates of ^{210}Po and ^{210}Bi are found to be in equilibrium.

Preface

The research presented in this thesis was conducted as part of the broader SNO+ collaboration. Any contributions or references not directly attributed to the author are explicitly acknowledged either here or within the text.

Chapters 2 and 3 provide a brief literature review of neutrino physics and an overview of the detector paper, respectively, as of the time of writing this thesis.

The data utilized in chapters 4, 5, and 6 when referred to as either "real" , "recorded" or "processed" (consisting of recorded events in the SNO+ detector, reconstructed for energy and position) originates from the data bank of the SNO+ collaboration and is not "recorded" or "processed" by the author.

It should be noted that the simulated flow discussed at the end of Chapter 5 is based on simulations conducted by Dr. John D. Wilson.

It should also be noted that the theoretical beta decay energy spectrum of ^{210}Bi, employed in Chapter 6, is based on the cited repository.

The author's distinct contributions within the specified chapters are as follows:

In Chapter 4, the focus is on the development of the mis-reconstruction detection algorithm for the SNO+ experiment. The author's work encompasses the formulation of relevant probability density functions (PDFs), configuration of the likelihood test, and testing.

Chapter 5 involves an analysis of flow patterns and flow rates of ^{210}Po in the SNO+ detector. The work presented here is by the author.

Chapter 6 details modifications and convolutions applied to the theoretical energy spectrum of ^{210}Bi to match what is seen in the SNO+ detector, alongside an explo-

ration of the distinct activity rates of Bismuth and Polonium 210. This work is done by the author.

Acknowledgements

I would like to express my gratitude to all those who have supported me throughout the journey of completing this thesis.

First and foremost, I extend my deepest appreciation to my supervising professor, Aksel Hallin, whose unwavering guidance, insightful ideas, and invaluable time have been instrumental in shaping the outcome of this work.

I am also indebted to the members of the SNO+ ualberta group for their support and constructive inputs during our weekly group meetings. My sincere thanks go to Dmytro Minchenko, Ankit Gaur, David Auty, John Wilson, Shaokai Yang, Jie Hu, Yang Zhang, Carsten Krauss, and Juan Pablo for their collaborative spirit and contributions.

I extend my gratitude to the esteemed committee members, Frank Hegmann and James Pinfold, for their invaluable time and efforts in critically evaluating my work, providing insightful revisions, and participating in the thesis defense process.

Furthermore, I would like to acknowledge the wider SNO+ collaboration for granting me access to essential computing resources and data, as well as the immeasurable guidance provided by numerous collaborators whose names are too numerous to list individually.

In summary, this thesis would not have been possible without the contributions and support of these remarkable individuals and groups. Thank you all for your influence on my academic journey.

Table of Contents

List of Figures

Chapter 1

Introduction:

The present thesis aims to investigate various aspects of background radiation that obscures the SNO+ experiment. It consists of three distinct analyses, all pertaining to the primary backgrounds and fundamental inquiries within the SNO+ experiment.

The SNO+ experiment, a collaborative effort, is poised to detect neutrinoless double beta decay by employing a heavy tellurium isotope in a scintillator liquid within a 12-meter diameter detector, viewed by approximately 9300 Photomultiplier tubes.

The subsequent chapters in this thesis serve the following purposes:

- Chapter 2 provides an overview of neutrino physics, including its historical development and the key questions and findings that are most relevant to both the SNO+ experiment and this thesis. This chapter serves to establish a foundational understanding of the background and its significance within the context of this experiment.

- Chapter 3 comprises a condensed detector paper dedicated to the SNO+ detector. It delves into the historical background of the SNO+ experiment and its predecessor (SNO), while providing an overview of the detector's construction, hardware, and software aspects. Furthermore, the chapter elucidates the relevant background interactions originating within the detector.

- Chapter 4 constitutes the first of the three analyses conducted in this thesis. It explores the phenomenon of light attenuation within the SNO+ detector

and presents a corresponding simulation. Additionally, the chapter addresses a significant source of position reconstruction errors, namely the total internal reflection of light on the detector surface. A classifier is developed to detect mis-reconstructed event positions, and its efficacy is explicated through detailed explanations and results.

- Chapter 5 investigates a specific point in the detector's event collection timeline where an influx of material is observed. The origin of this material is explored, and an estimation of its flow pattern and flow rate is provided.

- Chapter 6 involves the separation of event signals from the two most prevalent backgrounds within the detector. This analysis aims to determine the event rate for each of these two backgrounds, thereby enhancing our understanding of their impact on the SNO+ experiment.

By addressing these research questions and objectives, this thesis seeks to advance our knowledge of the background radiation influencing the SNO+ experiment.

Chapter 2

Neutrino Physics

Investigating the presence of neutrino-less double beta decay ($0\nu\beta\beta$) holds great importance within the field of particle physics, as its confirmation would challenge the conservation of lepton number, indicating physics beyond the Standard Model and providing crucial insights into neutrino properties and mass generation mechanisms. Multiple research groups are devoted to investigating the existence of this process, and its observation is the primary motivation of the efforts at the Sudbury Neutrino Observatory's experiment SNO+.This section aims to establish a solid foundation by presenting an introductory exploration of the concept of neutrinos. The theoretical framework of $0\nu\beta\beta$ will then be elucidated and insight into its importance will be explained.

2.1 Neutrinos

Neutrinos, categorized as fundamental particles within the lepton family, exhibit an extraordinary elusiveness due to their extremely weak interaction with matter, rendering their detection exceedingly challenging. They were first proposed in 1930 by Wolfgang Pauli who set the theoretical foundation for their existence [1]. In beta decay, the process by which nuclei emit an electron, the energy and momentum of the resulting beta particle does not match the original nucleus. To solve this discrepancy, Pauli hypothesized the existence of a new particle that was not detected. He coined

this particle a "neutron" originally, referring to its charge-less nature. However this name was already being used to refer to a different particle and Enrico Fermi later changed the name of this particle to the "neutrino" we know today, which means "little neutral one" in Italian [2].

Neutrinos are generated through diverse astrophysical and nuclear mechanisms, including stellar fusion reactions, supernova explosions, and the well-known radioactive decay of isotopes, as initially theorised by Pauli [3]. Due to their inherent weak interaction with matter, neutrinos possess the remarkable ability to effortlessly traverse through substances, exhibiting minimal absorption or scattering. Consequently, neutrinos emerge as invaluable tools for investigating astrophysical phenomena and even exploring the depths of the Earth's interior.

Neutrinos were finally first observed by Clyde Cowan and Frederick Reines in 1956. These neutrinos were produced in a nuclear reactor and observed directly in their experiment. This discovery was a significant breakthrough in the field of particle physics, earning Cowan and Reines the Nobel Prize in Physics in 1995 [4].

Since then neutrinos have been a hot topic of research and much work has been conducted to study their properties and behavior. This has led to many discoveries and insights into particle physics, astrophysics, and cosmology. Of the most significant of these, contrary to what was initially predicted by the Standard Model of particle physics experiments at the SNO and Super-Kamiokande Collaboration have separately shown that neutrinos have mass.[5, 6] This has in turn led to further investigations into neutrino mass and its implications for the behavior of other particles.

2.1.1 Neutrino Flavours

Neutrino are extremely difficult to detect and it took several decades to detect all three types of neutrinos: the electron neutrino, muon neutrino, and tau neutrino.

In their quest to locate the antineutrino emitted from a nuclear reactor, Frederick Reines and Clyde L. Cowan encountered the electron neutrino [4]. To accomplish the

detection of neutrinos, a substantial scintillator detector was utilized to observe the interactions of neutrinos with protons within the scintillator substance.

Subsequently, in 1962 at the Brookhaven National Laboratory, the detection of the muon neutrino transpired. The experiment employed a proton beam at the Alternating Gradient Synchrotron (AGS). The AGS's proton beam was directed onto a beryllium target and was made to produce in pi mesons. These pi mesons then in turn decay into muons and neutrinos that traveled 70 feet to strike a 5000 ton wall of steel built out of battleship plates. Due to their exceptionally feeble interaction properties, the neutrinos traversed through a steel barrier and entered a neon gas detector, where they collided with aluminum plates, generating discernible muon paths that could be observed and monitored within the gas chamber. This groundbreaking utilization of a neutrino beam not only marked a significant milestone but also served as a catalyst for subsequent investigations involving neutrino beams at AGS.

The consequential impact of this discovery was acknowledged through the prestigious recognition of the 1988 Nobel Prize awarded to Melvin Schwartz, Leon Lederman, and Jack Steinberger [7].

Tau neutrinos were the last to be discovered. Scientists at the Direct Observation of the Nu Tau (DONuT) collaboration inside FERMILAB finally detected tau netrinos in 1975. The setup of the DONuT experiment consisted of an 800-GeV proton beam produced by the Tevatron which was directed onto a beam dump made of tungsten alloy. This collision produced a hadron shower that subsequently decays partly into tau neutrinos. The tau neutrinos were deduced to have been produced using a nuclear emulsion target, as scintillating fiber tracker and a spectrometer [8].

2.1.2 Neutrino Oscillations and Mass Hierarchy

Although significant advancements have been made in neutrino experiments, several aspects of neutrinos, including their absolute masses and whether they possess Majorana or Dirac nature, remain unresolved.
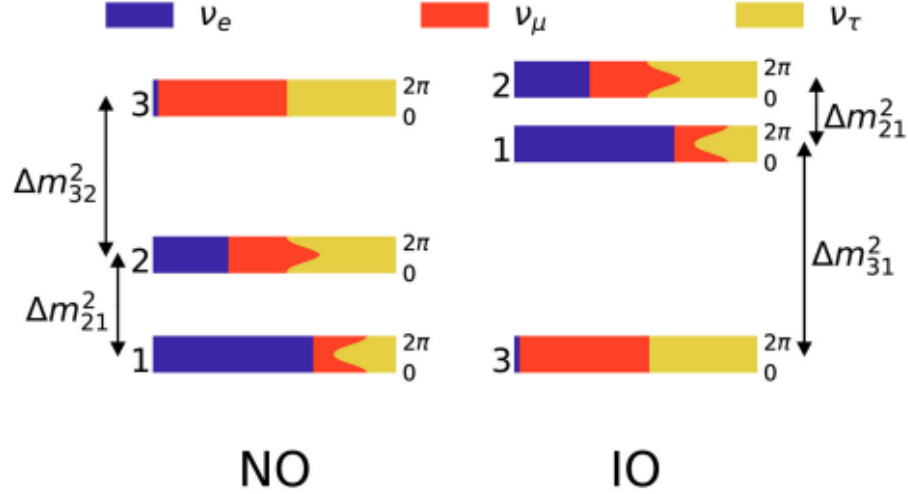
Figure 2.1: Neutrino mass hierarchies in the Normal Ordering (left) and Inverted ordering (right) [9]

The phenomenon known as neutrino oscillation elucidates that neutrinos of one flavor can undergo a transformation, converting into a different flavor while traveling through space. Through the observations of neutrino oscillation, valuable insights have been gained regarding the squared mass differences,Δm_{21} and $\Delta m_3 1$ ($\Delta m_{ij} = m_i - m_j$) of the three neutrino mass state, which represent the disparities in mass among the three distinct neutrino states.

The squared mass difference Δm_{21} has been observed to be greater than zero, however the sign of the squared mas difference Δm_{31} is as of yet unkown [9].

The neutrino mass hierarchy refers to the ordering of these mass eigenstates. There are two possible hierarchies that can be inferred from this. The normal hierarchy, where the three mass eigenstates are ordered such that $m1 < m2 < m3$, or the inverted hierarchy, where the ordering is $m3 < m1 < m2$. The true hierarchy is important because it impacts the probability patterns of neutrino oscillations.[10]

In the normal hierarchy, $\Delta m_{21}^2 = 7.5x10^-5eV^2$ and $\Delta m_{31}^2 = 2.5x10^-3eV^2$ and In the inverted hierarchy, $\Delta m_{21}^2 = 7.5x10^-5eV^2$ and $\Delta m_{31}^2 = -2.5x10^-3eV^2$

2.1.3   The See-Saw Mechanism

There is still much that is not known about neutrinos, including their exact masses and whether they are Dirac or Majorana particles.

In the Standard Model, neutrinos are considered to be Dirac particles, which means that they have a distinct antiparticle with opposite quantum numbers. In the case of Dirac neutrinos, they can be represented by a two-component spinor, encompassing both their particle and antiparticle states. Conversely, if neutrinos are Majorana particles, they are unique in that they are their own antiparticles, and their representation requires a single-component spinor. This fundamental distinction carries profound consequences in the realm of neutrino physics [11].

The seesaw mechanism is a theoretical framework that seeks to explain the small masses of neutrinos in terms of new physics beyond the Standard Model. This mechanism assumes that neutrinos are Majorana particles, and it introduces heavy right-handed neutrinos that interact with the Standard Model neutrinos via Yukawa couplings. The mass matrix for the neutrinos can then be written as:

$$\begin{pmatrix} 0 & m_D \\ m_D & M_R \end{pmatrix} \tag{2.1}$$

where m_D is the Dirac mass term that couples the left-handed and right-handed neutrinos, and M_R is the Majorana mass term for the heavy right-handed neutrinos. Within this framework, the relatively small masses of neutrinos in the Standard Model stem from the interplay of mixing between light and heavy neutrinos, a relationship governed by the ratio of the Dirac and Majorana mass terms.

The likelihood of neutrinoless double beta decay is contingent upon the square of the effective Majorana mass of the neutrino, which is directly proportional to the extent of mixing between the light and heavy neutrinos. Mathematically, the effective Majorana mass can be expressed as follows:

$$m_{\beta\beta} = |\sum_i U_{ei}^2 m_i| \tag{2.2}$$

where U_{ei} is the mixing matrix element between the electron neutrino and the ith mass eigenstate, and m_i is the mass of the ith eigenstate.[12]

If the seesaw mechanism is correct, then neutrinos can participate in $0\nu\beta\beta$ decay. Detecting this phenomenon would provide unequivocal evidence supporting the hypothesis that neutrinos possess the characteristic of being Majorana particles. The current upper limit on the effective Majorana mass from $0\nu\beta\beta$ experiments is in the order of 10s-100s of meV, which is consistent with the idea that neutrinos are Majorana particles with masses around the sub-eV scale. [13–15]

2.2 Double Beta Decay

2.2.1 Two Neutrino Double Beta Decay

Two neutrino double beta decay ($2\nu\beta\beta$) is a rare nuclear process that occurs when a nucleus undergoes beta decay emitting two electrons and two antineutrinos. The process can be described by the following equation:

$$(A, Z){-}{>} (A, Z+2) + 2e^- + 2\bar{\nu}_e \tag{2.3}$$

where (A,Z) represents the parent nucleus, and (A,Z+2) represents the daughter nucleus. The electrons that are released are commonly referred to as beta particles, while antineutrinos represent the counterparts of neutrinos.

$2\nu\beta\beta$ is a second-order weak process that is allowed in the standard model of particle physics.[16] It is mediated by the exchange of two virtual W bosons, as shown in the Feynman diagram below:

Up to this point, the occurrence of two-neutrino double beta decay has been detected in various isotopes, such as 76Ge, 130Te, 136Xe, and 150Nd. Among these, the
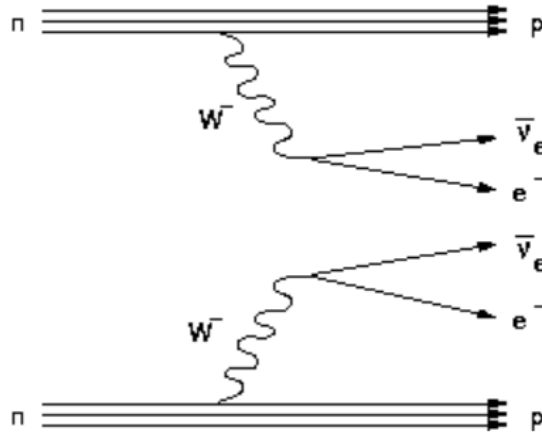
Figure 2.2: Feynman diagram of $2\nu\beta\beta$ [17]

most extensively studied is 76Ge. The GERDA and Majorana Collaborations have undertaken experiments aimed at detecting $2\nu\beta\beta$ decay in 76Ge by utilizing extensive arrays of high-purity germanium detectors positioned in deep underground locations, thereby minimizing background interference. These experiments have provided some of the most stringent limits on the half-life of $2\nu\beta\beta$ decay.[18]

2.2.2 Neutrinoless Double Beta Decay

Neutrino-free dual-beta decay ($0\nu\beta\beta$), postulates a nuclear event wherein a nucleus experiences beta decay, releasing a pair of electrons devoid of any accompanying neutrinos. The aforementioned occurrence can be mathematically depicted as:

$$(A, Z) - > (A, Z + 2) + 2e^- \tag{2.4}$$

$0\nu\beta\beta$ decay is a rare, second-order weak process that is not allowed in the standard model of particle physics. However, it is predicted to occur if neutrinos are their own antiparticles (i.e., Majorana particles). An absence of neutrinos could potentially arise from the interaction of virtual particles during the occurrence of two beta decays [19].

Illustrated here is the Feynman diagram representing the decay process of $0\nu\beta\beta$.
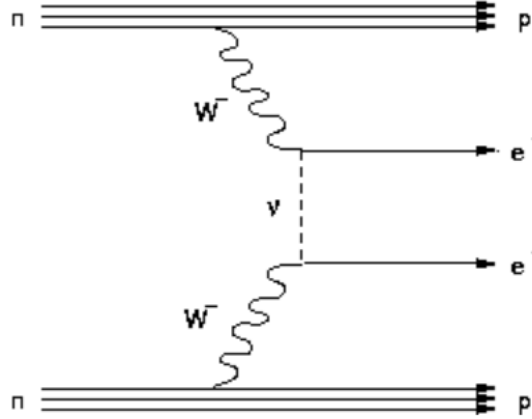
Figure 2.3: Feynman diagram of $0\nu\beta\beta$ [17]

Several experiments are currently underway to search for $0\nu\beta\beta$ decay, including the SNO+, CUORE, GERDA, KamLAND-Zen, and EXO-200 experiments. These experiments use various techniques to minimize background noise and detect the extremely rare event of $0\nu\beta\beta$ decay. The search for $0\nu\beta\beta$ decay is a highly active area of research in both particle physics and nuclear physics, and the observation of this process would represent a major breakthrough in our understanding of fundamental particles and their interactions. [20]

Chapter 3

SNO+

Located around 2,000 meters below the surface in an operational nickel mine close to Sudbury, Canada, lies the SNO+ experiment—a large-scale neutrino detector boasting a kilo-tonne capacity and designed to minimize background noise. This remarkable detector was obtained from the renowned SNO experiment, which played a pivotal role in unraveling the solar neutrino problem by detecting all three flavors of neutrinos and validating the theory of neutrino oscillation. The success of the SNO experiment led to the establishment of SNOLAB, a level 2000 clean lab facility that hosts several experiments, including SNO+. The SNOLAB clean enviroment prevents radioactive contamination from the surrounding rocks and mine dust, allowing low backgrounds for all experiments.

SNO+ has three phases, each distinguished by different material filling the main detector volume.SNO+ benefits from its expansive dimensions, enabling substantial isotope exposure on an annual basis, while its minimal background rates contribute to a high anticipated discrimination regarding $0\nu\beta\beta$. In this section, we commence with an outline of the detector's structure, encompassing its architectural design, hardware components, software systems, and the diverse physics stages undertaken throughout the experiment.

3.1 Detector Overview

The SNO+ detector is designed to detect rare interactions that require sensitive experiments located at SNOLAB, shielded from the cosmic muon flux by the ~2,000 meter rock cover. An outline of the SNO+ detector is shown in shown in Figure 3.1

The components of the SNO+ detector include:

- A large acrylic vessel (AV), 6 meters in radius, filled with a Linear Alkyl Benzene (LAB) and 2,5 diphenyloxale (PPO). The LAB is the solvent while PPO serves as the fluor. The AV is viewed by approximately 9,300 photomultiplier tubes (PMTs) that are mounted on a stainless steel support structure (PSUP) which is 18m in diameter.

- In order to shield the AV from radiation from surrounding rocks and detector components, the experiment employs a cavity consisting of an outer and an inner cavity submerged in ultra-pure water. This ultra pure water is a highly purified water that has been meticulously treated to remove impurities. The inner cavity holds 1,700 tonnes of ultra-pure water, while the external cavity contains 5,700 tonnes of ultra-pure water. This arrangement provides optimal shielding and ensures accurate measurements of particle interactions within the AV.

- To keep the AV secure, the experiment utilizes two sets of high-purity Tensylon ropes. The hold-up ropes (HUR) suspend from a deck above the water volume and are hooked to ridges in the AV, while the ropes (HDR) hold the vector down and are attached to the bottom of the cavity. This ensures that the AV remains stable and motionless during data collection.

- The experiment also includes a scintillator and tellurium purification plant located at SNOLAB. Telelrium is used as it is a potential candidate to undergo neutrinoless double beta decay . The plant facilitates the filling of purified LAB

and tellurium into the detector. The purification system ensures that the LAB and tellurium are free of any impurities that could interfere with the detection of particles in the AV.
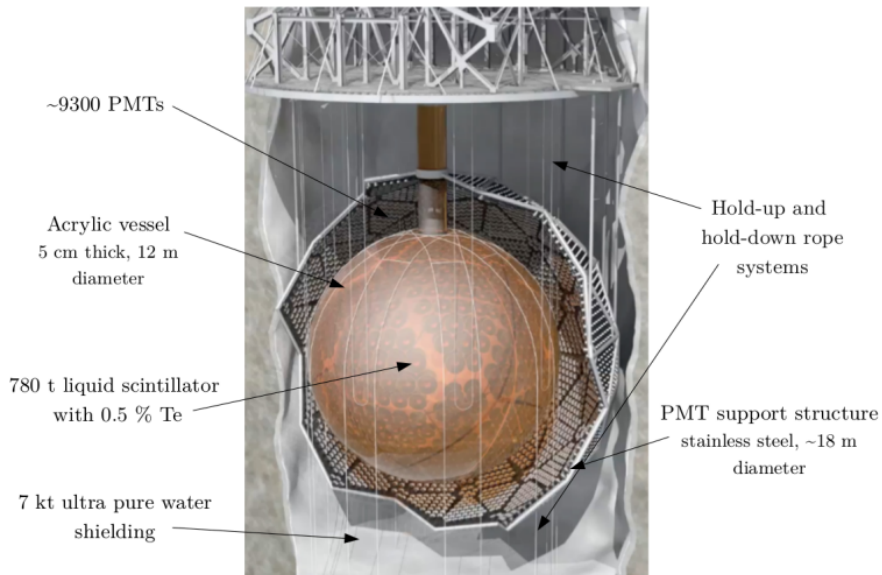
Figure 3.1: Schematic of the SNO+ detector with its major components labelled, taken from [21]

The SNO+ detector is housed in a 22-meter-wide and 34-meter-tall cavity and enclosed within a layer of "ultra-pure" water. This shields the detector against the detrimental influence of both cavernous rock and the radioactivity emitted by the radioactive isotopes in the construction material of the PMTs.

A more in depth and holistic overview of the detector can be found at [22]

3.2   Detector Phases

The prime objective of the SNO+ experiment is to examine the physics interactions that occur in the fiducial volume (FV), within the AV's inner liquid . A key feature of this setup is the ability to easily modify or replace the liquid, which allows for a diverse range of physics investigations. Additionally, by examining the detector model and experimental backgrounds beforehand, researchers can prepare for the introduction of

the isotope. Every experiment phase is marked by the change of the material inside the Fiducial Volume. This section presents an outline of the proposed phases and their respective goals.
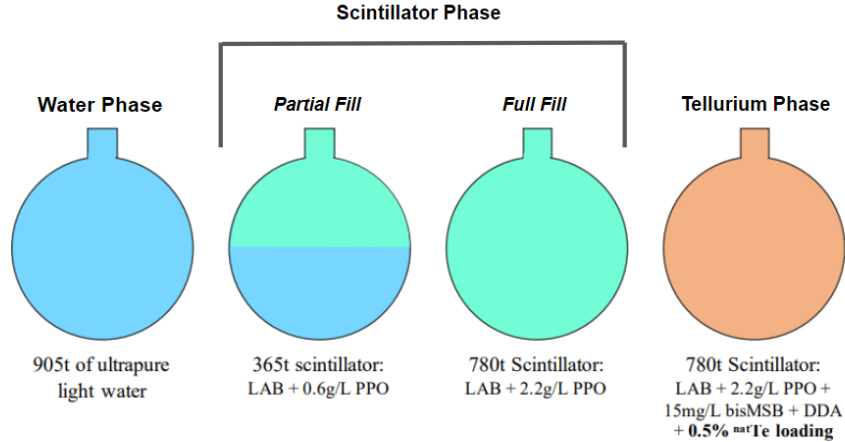
Figure 3.2: Phases of the SNO+ experiment, adapted from [23]

3.2.1 Water Phase

Between December 2016 and July 2019, the SNO+ detector operated as a water Cherenkov detector filled with 905 tonnes of ultra-pure water. The water phase allowed for optical calibration of the detector, characterization of external background contributions, and detection of Cherenkov radiation emitted by relativistically charged particles. Invisible nucleon decay was the explored during this detector phase and lower limits on neutron and proton lifetimes were set [24]. The flux of 8B solar neutrinos was also measured, demonstrating low levels of backgrounds[25]. Various other aspects were also examined including optical properties, response of the photomultiplier tubes (PMT), and background measurements to assess the external backgrounds originating from the water volume and the hold down ropes that are particularly important for the Double beta decay (Tellerium) phase. LAB-PPO was added to the detector at the end of the water phase, intiating the Scintillator phase.

3.2.2 Scintillator (Calibration) Phase

This analysis in this thesis will focus on analyzing the scintillator phase of the SNO+ experiment. This phase involves replacing the heavy water in the AV with 78 tonnes of organic liquid scintillator. This liquid scintillator is composed of linear alkylbenzene (LAB) and 2,5-diphenyloxazole (PPO), which serves as the fluor. [26]

The decision to use LAB was based on many factors including its compatibility with acrylic and high light yield. [27]

This "unloaded" scintillator phase, which doesn't include the double β isotope, will allow for the measurement of the radiopurity of the SNO+ scintillator. During this phase, the optical model and detector response will be assessed, and the scintillator mixture's radioactive background levels will be evaluated. The detection of low energy solar neutrinos, reactor and geo anti-neutrinos, and potential supernova neutrinos will be also be possible during this phase.

Filling of the LAB started in October 2018 and this phase will continue until the addition of Tellurium.

3.2.3 Tellurium Phase

This, final, phase of the SNO+ experiment will involve loading a proposed 10-20 tonnes of Tellerium into the FV. This Tellerium will serve as the isotope to detect $0\nu\beta\beta$. The Tellerium will be processed at the processing plant adjacent to the detector to reduce long-lived isotopes generated by cosmic ray spallation reactions, followed by filtration and two recrystallizations to remove contaminants.[27] This phase has yet to begin.

3.3 Radon 222, Lead 210 and daughters

The SNO experiment went through a construction phase from 1994 to 1998 and was later drained in 2006 before being refilled for the SNO+ phase in 2016. During this

time, the inner surface of the AV was exposed to mine air, which included airborne ^{222}Rn that decayed, with daughters depositing on the inner surface of the AV. This led to a layer of ^{210}Pb on the surface of the AV with a long half life of ~ 22 years. Due to its long half life, this ^{210}Pb still exists in large amounts in the detector. While ^{210}Pb is not a detectable background in the detector, ^{210}Pb decays into ^{210}Bi and in turn ^{210}Po. These daughters can be a source of background for the SNO+ experiment as they leach into the detector medium or are mis-identified as being inside the detector medium by the SNO+ position reconstruction algorthim.
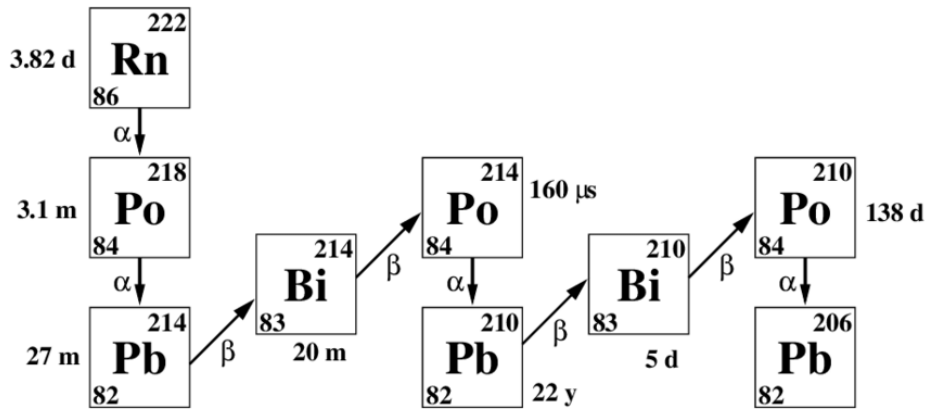
Figure 3.3: Decay chain of ^{222}Rn. [28]

The analyses in this thesis focus on understanding the ^{210}Bi and ^{210}Po in the detector. It is important to study and understand these backgrounds in order to accurately interpret the data from the SNO+ experiment. More information on backgrounds can be found in the official SNO+ experiment overview paper here. [22]

3.3.1 Bi210 & Po210

The decay of ^{210}Po originating from ^{210}Bi constitutes the most prevalent background event in the SNO+ experiment. Understanding the behavior of ^{210}Po in the detector holds crucial importance due to its dominance, with an event rate of $(2.4\pm0.8)\,\mathrm{Bq/m^2}$, surpassing all other background sources.

When alpha particles emitted from the decay of ^{210}Po interact with atoms in the scintillator, they can generate free neutrons. These can then be captured by a carbon

nucleus which creates a background that falls within the $0\nu\beta\beta$ decays' ROI.[22, 29]

3.4 Event Simulation and Reconstruction

To comprehensively understand the events in the SNO+ detector, it is necessary to have a holistic understanding of the detector's geometry and PMT response. To transform the PMT hits (nhits) into the reconstructed position and energy of the event that caused them, various statistical algorithms and techniques are employed. These reconstruction algorithms are designed to extract maximum information from the signals detected by the PMTs. This information includes the direction and energy of particles, along with their timing and signal pattern. Moreover, algorithms can be developed to distinguish between different particle types based on event coincidences interactions.

In this subsection, an general overview of the Monte Carlo simulations used to explore the detector's response and build the algorithms employed for identification will be given. Subsequently, the effectiveness of the position reconstruction algorithm, used extensively in this analysis, will be discussed.

3.4.1 Monte Carlo Simulation

The SNO+ experiment utilizes advanced Monte Carlo simulations to accurately model the behavior of particles in the detector. The simulations are handled by Geant4, which simulates all physical processes including light emission, scattering, absorption, and PMT response [30].

A detailed architecture of the detector and all its components is implemented in the software. An event generator is employed to simulate a particular event and its location and this has been implemented for multiple physics interactions and backgrounds, including radioactive decays, solar and reactor neutrinos, and calibration sources. Once an event is generated, the simulation will propagate the resultant particles and any light they in turn generate from the original point of simulation through

their travelled paths up to the point of detection by the PMT. Finally, the front-end electronics, trigger system, and event builder are simulated and the same reconstruction algorithms used on real events can be applied. This allows for experimentation with the simulation of Monte Carlo data and tweaking of the simulation algorithms to match what is seen in the detector with real events.

More information on the simulation and analysis software can be found in [31]

3.4.2 Position Reconstruction

Reconstruction algorithms are used to determine the position, energy and time of events within the detector. These algorithms are customized for each experimental phase, as the active medium's light production mechanisms differ. The first quantities reconstructed are the initial position and time of the events, based on timing information from triggered PMTs and their locations. The position reconstruction algorithms assume that photons are produced at a single point at a specific time and then use straight-path trajectories from the source point to the hit PMTs to calculate arrival times. A log likelihood is calculated by comparing measured hit times to a probability density function (PDF) derived from Monte Carlo simulations. The algorithm then utilizes the Powell optimization algorithm to identify the event's position and time, maximizing the log-likelihood function. This function is defined as the sum of the logarithms of the probability density function for each hit. [22,30]

The resolutions of the position reconstruction algorithm for the full fill scintillator phase are shown in 3.4
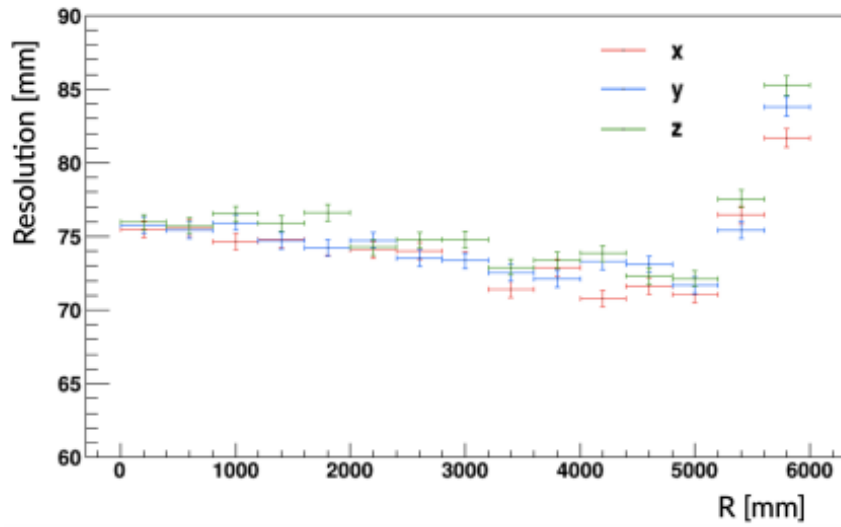
Figure 3.4: Position resolution in the full fill scintillator phase as a function of distance from the center (R) of the detector in the x, y and z directions [32]

Chapter 4

Position Mis-reconstruction from the Acrylic Surface :

This section of the thesis provides an analysis of optical effects in the SNO+ detector. Firstly, the most common events and their energy spectra will be summarized briefly. The section will then focus on the attenuation of light that occurs in the detector by looking at ^{210}Po events. A toy model for this attenuation will be presented and compared with the attenuation observed in the detector.

Following this, the section will delve into the issue of misreconstruction of events that originate on the acrylic surface but are mistakenly reconstructed into the fiducial volume. This problem will be discussed, and a method for detecting such events will be explained. This method will involve looking at optical effects in the detector, particularly total internal reflection.

The section will conclude by presenting the results and effectiveness of this method for detecting misreconstructed events. This will be done through a thorough analysis of the data and a discussion of the implications of the findings.

4.1 Energy Spectra

The SNO+ experiment observes three background isotopes with high abundance: ^{210}Po, ^{210}Bi, and ^{14}C. Decay energies and schemes taken from [33]

^{210}Po undergoes almost 100% alpha decay to ^{206}Pb, with an associated energy of

5304.337keV, a branching ratio of 100% and a half life of ~ 138 :

$$\text{Decay Scheme: } {}^{210}\text{Po} \rightarrow {}^{206}\text{Pb} + {}^{4}He$$

$$\text{Endpoint Energy: } 5304.337keV$$

$$\text{Branching ratio: } 100\%$$

^{210}Bi decays almost exclusively by beta decay to ^{210}Po, with an endpoint energy of 1162.8keV, a branching ratio of 100% and a half life of ~ 5 days:

$$\text{Decay Scheme: } {}^{210}\text{Bi} \rightarrow {}^{210}\text{Po} + \beta^{-}$$

$$\text{Endpoint energy: } 1162.8keV$$

$$\text{Branching ratio: } 100\%$$

Similarly, ^{14}C decays via beta decay to ^{14}N with an endpoint energy of 156.475keV, a branching ratio of 100% and a half life of $\sim 5{,}730$ years:

$$\text{Decay Scheme: } {}^{14}\text{C} \rightarrow {}^{14}\text{N} + \beta^{-}$$

$$\text{Endpoint energy: } 156.475keV$$

$$\text{Branching ratio: } 100\%$$

The number of photo-multiplier tubes (PMTs) registering light from the decay products, referred to as "Nhits," is approximately proportional to the energy of the event. The endpoint energy of the beta decay spectrum of ^{210}Bi corresponds to $\sim$380 nhits, while the spectrum of ^{14}C covers the 0-50 nhit range. The alpha decay of ^{210}Po results in a single energy output, but due to various systematic uncertainties such as alpha quenching, attenuation at different positions in the liquid, and lack of PMT coverage, we observe a Gaussian energy spectrum centered at $\sim$130 nhits, as shown in Fig. 4.1.
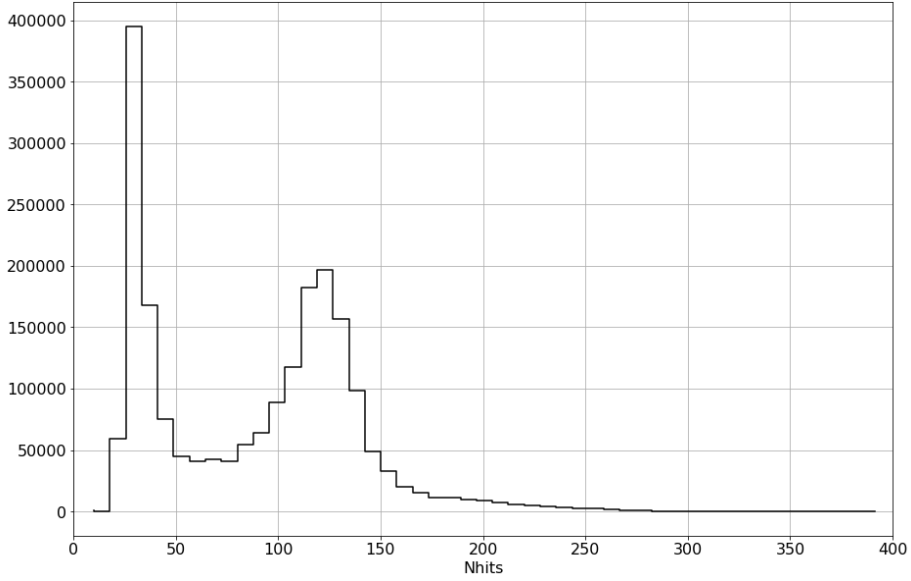
Figure 4.1: Energy spectrum of the background events ^{210}Po, ^{210}Bi, and ^{14}C, as reconstructed from the number of PMT hits (Nhits)

The ^{210}Pb decay, from which ^{210}Bi originates, cannot be directly detected as its endpoint energies are below the reconstruction threshold limits. An example of a theoretical beta decay energy spectrum and the reconstruction nhit threshold is shown in 4.2.
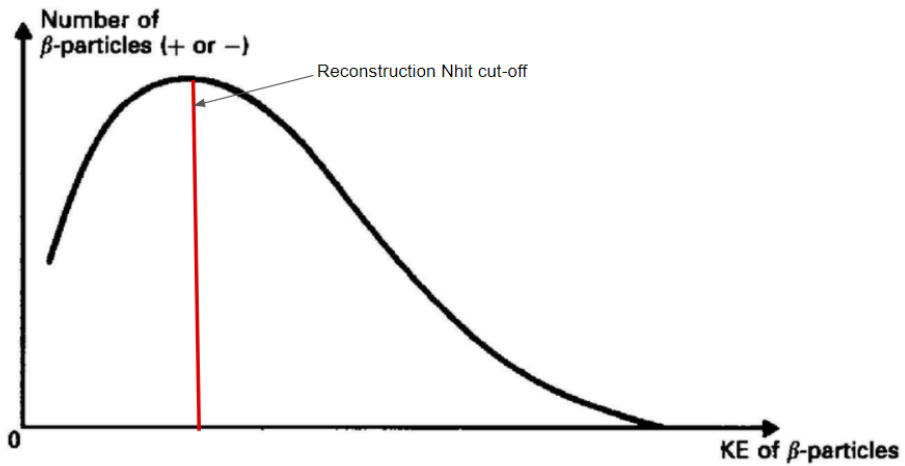
Figure 4.2: Theoretical Beta Decay energy spectrum showing where the reconstruction cut would be applied. Adapted from [34]

4.2 Attenuation

The attenuation of light in liquid is a fundamental aspect of many experimental and technological applications. Light in the detector can be influenced by several physical mechanisms, including absorption, scattering, and reflection. Absorption occurs when photons from the light are absorbed by the molecules or atoms in the liquid, leading to a reduction in light intensity. Scattering occurs when photons interact with particles or molecules in the liquid, causing the photons to change direction and become diffused. Reflection occurs when light is reflected off the surface of the liquid, contributing to the overall attenuation of the light. A thorough understanding of light attenuation in a liquid is crucial for the design and optimization of experiments that rely on light detection, as well as for the development of efficient optical communication systems. Therefore, studying the attenuation of light in liquid is of great interest to researchers across various disciplines.

Here, attenuation by absorption will be discussed in the liquid and verified by observation. This attenuation can be described by Beer Lambert's law: $I(z) = I_0 e^{-\alpha z}$

where $I(z)$ is the intensity of light at a distance z from the entrance point into the liquid, I_0 is the initial intensity of the light, and α is the absorption coefficient of the liquid. The absorption coefficient determines how far light can travel in a material before being absorbed and quantifies how effectively a material absorbs light. The equation shows that the intensity of the light decreases exponentially with increasing distance traveled due to absorption.

4.2.1 Attenuation of Photons Created by Polonium 210

In the fiducial volume of the detector, light from ^{210}Po undergoes attenuation through absorption, which is correlated with its decay position. The attenuation behavior of ^{210}Po is depicted in Figure 4.3 as a function of radius. The figure reveals that the mean value of the polonium peak increases as the radius increases. To remove ^{14}C

events, an nhit cut of 80 is imposed. Unlike ^{210}Po, ^{210}Bi is mainly localized on the acrylic surface and does not diffuse into the fiducial volume. However, ^{210}Bi events can misreconstruct into the fiducial volume at higher radii, and this issue will be discussed in Section 4.3.
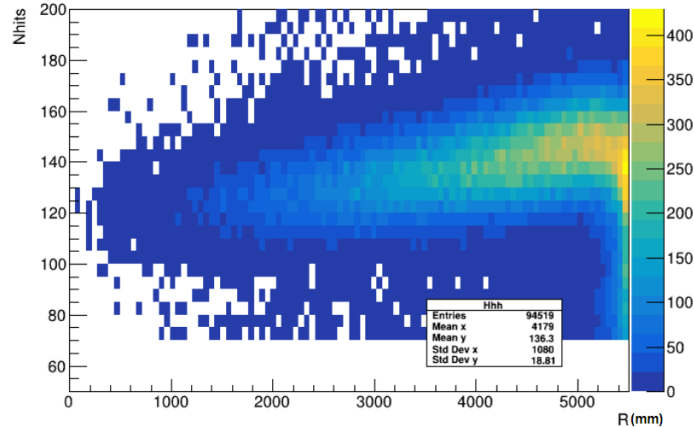
Figure 4.3: Two dimensional histogram with a cut at 80 nhits. Attenuation of the Polonium peak can be seen. This occurs because events closer to the detector surface emit light that travels shorter distances on average through the liquid. As a result, this light is less prone to being absorbed on average. Light emitted from events further than 5.3m of the detector center can undergo total internal reflection, causing the dip seen in nhits at large radii.

4.2.2   Toy Simulation of Attenuation

A Python-based toy model was developed to simulate the attenuation of ^{210}Po. The model begins by generating events uniformly throughout a sphere with a radius of 6m, representing the acrylic volume. This process involves generating random numbers from a uniform distribution and mapping them to spherical coordinates. Specifically, for each event, a random number is generated for ϕ from the range $(0, 2\pi)$, for $\cos(\theta)$ from (-1, 1), and for a variable u from (0, 1). The value of $\cos(\theta)$ is then inverted to obtain θ, while u^3 is multiplied by 6 to obtain a random and uniformly distributed selection of the radius.

Mathematically, the random coordinate selections for an event are as follows:

$$\phi = \text{np.random.uniform}(0, 2\pi) \tag{4.1}$$

$$\theta = \cos^{-1}(\text{np.random.uniform}(-1, 1)) \tag{4.2}$$

$$r = 6 \times \sqrt[3]{\text{np.random.uniform}(0, 1)} \tag{4.3}$$

In the above equations, np.random.uniform refers to a Python package that generates random numbers from a uniform distribution within the specified range. This ensures that the events are distributed uniformly throughout the sphere, with their occurrence scaling with the cube of the radius (r^3). Plots illustrating these events and their occurrence varying with the radius are depicted in Figure 4.4.

The next step involves attenuating these events based on their position within the liquid. This attenuation can be achieved by selecting an attenuation length from a distribution derived from the Beer-Lambert law. The attenuation length (a) is calculated using the equation:

$$a = \log(\text{np.random.uniform}(0, 1))/ - \alpha \tag{4.4}$$

Additionally, approximately 130 photons (nhits) of light can be simulated to travel in random directions from each event. These directions are obtained using the following procedure:

$$v = \text{np.random.rand}(3) \times 2 - 1 \tag{4.5}$$

$$v/ = ||v|| \tag{4.6}$$

Let's break down the steps involved:

- np.random.rand(3) generates a random array of three numbers between 0 and 1, following a uniform distribution. Each number represents a component of the 3D vector.

- The array generated in the previous step is multiplied by 2 and then subtracted by 1 ($\times 2 - 1$). This scaling operation transforms the range of the values from [0, 1] to [-1, 1]. Consequently, each component of the vector falls within the range of -1 to 1.

- $v/ = ||v||$ normalizes the vector v by dividing each of its components by its Euclidean norm. The function np.linalg.norm() calculates the Euclidean norm of a vector. This normalization process ensures that the resulting vector has a unit length. By dividing the vector by its norm, we effectively scale the vector to have a length of 1. The resulting vector, v, can be interpreted as representing a direction in 3D space

.

Following these steps, the simulated event, along with the directions of 130 photons (v_i) and their corresponding generated attenuation lengths (a_i), can be used to calculate the distance traveled by each photon in the liquid until it reaches the surface of the acrylic sphere.

For each of these photons v_i, if the distance travelled is larger than or equal to the thrown attenuation length a_i, this photon is considered attenuated and not registered in an events total nhits..

Total internal reflection plays a significant role in limiting the amount of light reaching the PMTs. When light undergoes total internal reflection, it becomes trapped inside the detector, repeatedly reflecting off the acrylic surface / water barrier indefinitely. To accurately model this behavior, the toy simulation inhibits light from crossing the acrylic surface into water if it strikes the detector at an angle greater than the critical angle. The critical angle θ_{critical} is found using Snell's law. For water $n_{\text{water}} = 1.33$ and for the surrounding acrylic and scintillator $n_{\text{scint}} = n_{\text{acrylic}} = 1.5$. So $\theta_{\text{critical}} = \sin^{-1}\left(\frac{1.33}{1.5}\right) \approx 62.5°$.

Utilizing Figure 4.5 as a visual reference, we can determine the distance from the
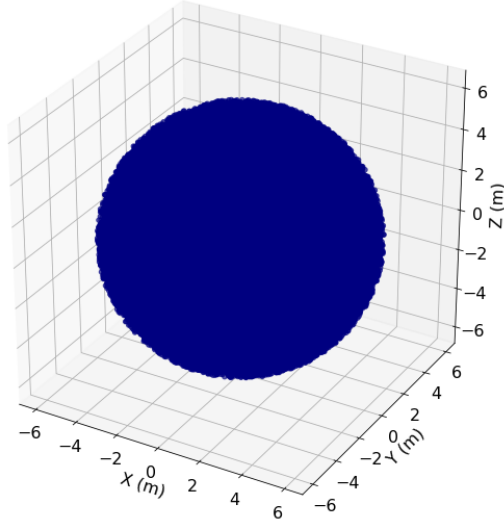
(a) Toy simulation event view
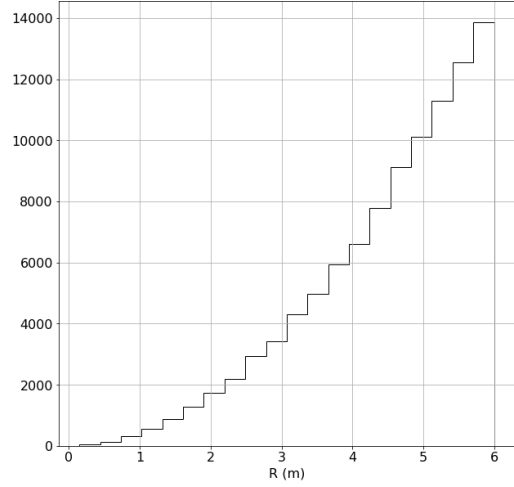
(b) Toy simulation radius distribution

Figure 4.4: Plots showing the simulated Polonium 210 events (a) in the toy simulation and the distribution of radius of events (b)

center of the detector at which an event must occur in order for the emitted light to potentially undergo total internal reflection upon striking the detector's surface. Consider an event within the detector positioned at a distance x from its center. The line connecting this event to the detector's center also has a length of x. Another line extends from the detector's center to the acrylic vessel, where a potential event could emit light that reaches the surface. This line, with a length of 6m, corresponds to the radius of the detector and acts as the normal reference.

Introducing two angles: θ_c, representing the angle of incidence of the light ray on the detector's surface, and θ_r, defined as the angle between the line connecting the event to the detector's center and the line linking the event to the acrylic vessel's surface where light might strike, as illustrated in Figure 4.5. By applying the sine rule, we establish $\frac{x}{\sin(\theta_c)} = \frac{6}{\sin(\theta_r)}$, yielding $\theta_c = \sin^{-1}\frac{x}{6\sin(\theta_r)}$. Consequently, the maximum angle θ_c at which a light ray can strike the acrylic surface depends on the event's distance from the detector's center, reaching its zenith when $\theta_r = 90°$.

Substituting 62.5° into this equation reveals that an event must be approximately 5.3 meters from the center of the detector to emit light capable of undergoing total

27

internal reflection. Figure 4.5 provides a visual representation of an event located at (5.3,0)m, emitting a light ray that strikes the surface at the critical angle. Logically extending this concept, events positioned even closer to the surface will emit light that can strike at even larger angles. As a result, events situated beyond the 5.3m radius from the detector's center will more frequently experience total internal reflection. This observation aligns with the noticeable mis-reconstruction prevalent in events occurring at radii greater than 5.3 meters, where emitted light often strikes the acrylic vessel or water barrier at angles surpassing the critical angle.
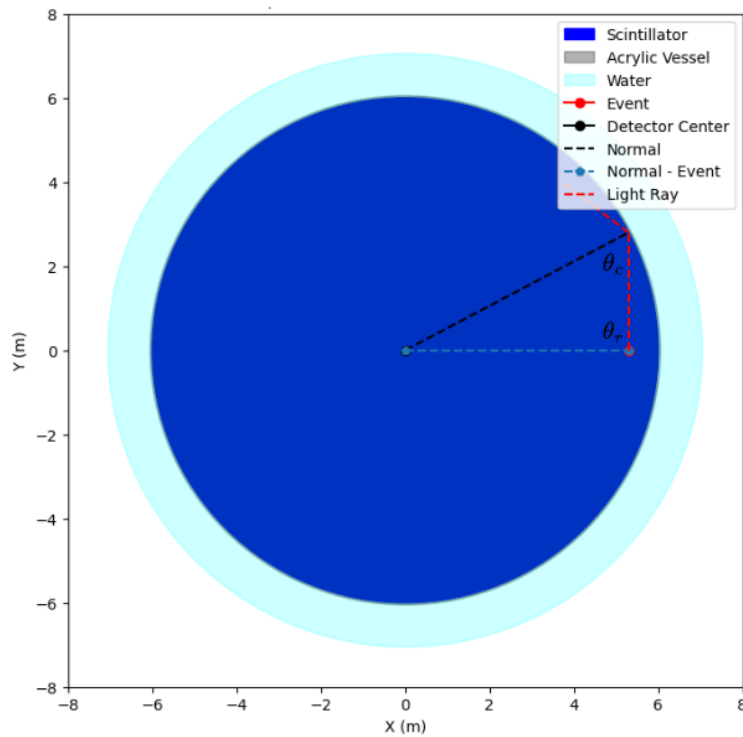
Figure 4.5: Schematic visualisation of the total internal reflection of a light ray emitted from an event near to the acrylic vessel striking the acrylic vessel at the critical angle.

Results

The toy model was executed to simulate 10,000 randomly generated events. In order to match the average of nhits vs radius between the simulated events, depicted in Figure 4.6a, and the events recorded in the detector that satisfy an 80 nhit cut, shown in Figure 4.6b, the attenuation length was systematically varied. A TProfile

histogram is a graphical representation used to depict the mean value of the variable Y and its associated error for each bin along the X-axis. In the context of this model, the TProfile of "nhits vs radius" signifies that the mean number of hits (nhits) is plotted as a function of the radius. This allows for the investigation of how the number of hits varies with different distances from the center of the detector.

By adjusting the attenuation length, a value of 16.1m was determined to attain this desired correspondence. The application of an 80 nhit cut reliably isolates the ^{210}Po peak from the signatures of ^{210}Bi and ^{14}C for events occurring within 5m. However, for events located at radii greater than 5m, factors such as total internal reflection on the acrylic surface of the detector compromise the functionality of the reconstruction algorithm. Consequently, this explains the observed disparity between the TProfile obtained from the events simulated in the toy model and the TProfile derived from the recorded data in this range.

4.3 Mis-reconstruction of Events on the Acrylic Vessel

Within the vicinity of the AV surface, optical phenomena, particularly total internal reflection, exert a significant influence on the trajectory of light emitted by an event. Consequently, the average angular distribution of PMTs hit by events near and within the AV differs noticeably from that of events occurring closer to the centre of the detector. SNO+'s reconstruction algorithm fails to account for this effect, resulting in misreconstruction of many events originating from near the AV but appearing closer to the center of the fiducial volume. The subsequent sections of this chapter will discuss this misreconstruction and its radial dependence and then a methodology will be presented to exploit the optical effects near the AV in order to discern the origins of FV-reconstructed events, particularly those originating from the AV.
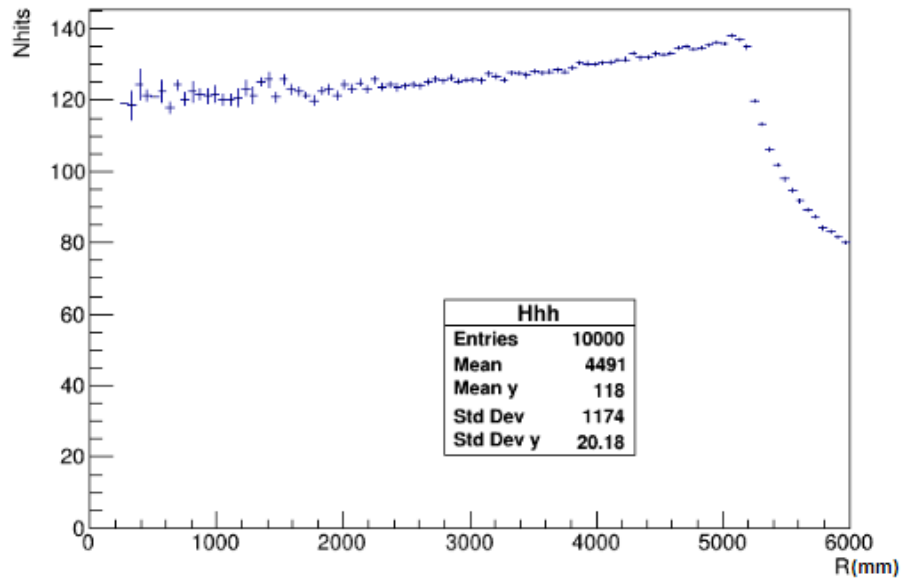
(a) Toy Simulation
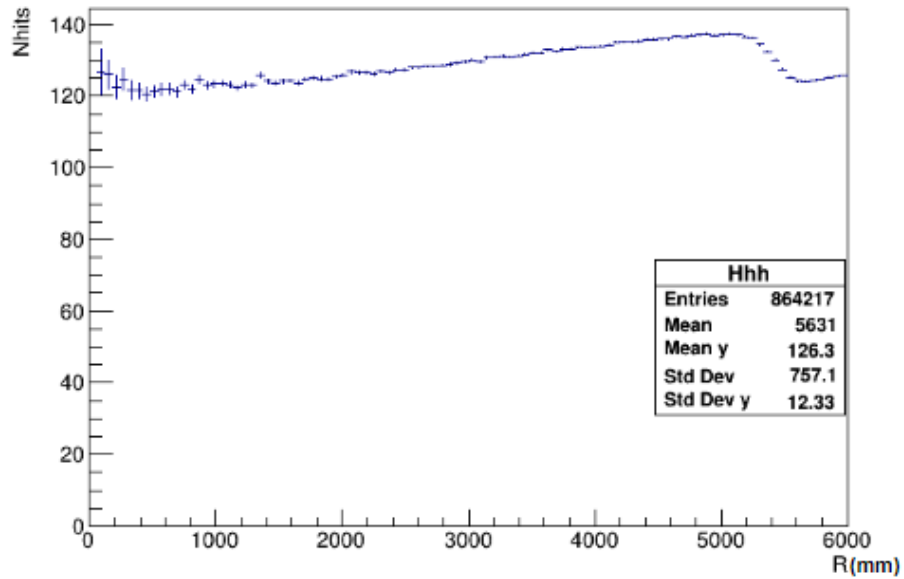
(b) Data

Figure 4.6: TProfile of the nhit spectrum for the toy simulation of Polonium 210 (a) and the nhit spectrum of events seen in data (b)

4.3.1 Total Internal Reflection

In the fiducial volume, events are observed that emit a certain number of photons, which are then detected by the PMTs. The positions of the PMTs that detect the emitted light are significantly influenced by the distance between the event location and the AV surface. Refraction occurs at the barrier separating the AV and the FV, and events closer to the AV surface emit light that strikes the AV surface at larger incident angles resulting in greater refraction. This effect leads to a distinct angular distribution of events between those occurring on the AV and those in the FV. In Figure 4.7a, we can define the angle formed by the reconstructed position of an event, the origin, and the hit PMT, to use as a proxy for viewing the impact of total internal reflection on the angular distribution of events. Figure 4.7b displays the angular distribution of these defined angles for events simulated within the FV and events simulated on the inside of the AV surface. A noticeable dip can be observed in the angular distribution of hit PMTs for events occurring on the AV surface, which can be attributed to total internal reflection, where light emitted from the AV surface is more likely to undergo this effect.

4.3.2 Radius Dependence

Misreconstructions of events occurring on the AV are more frequent closer to the AV itself than in deeper regions of the fiducial volume. Consequently, numerous analyses conducted at SNO+ employ a stringent fiducial volume cut of approximately 4 units, where the occurrence of misreconstructions is minimal. The detection of misreconstructed events would enhance the utilization of a larger portion of the fiducial volume, enabling the incorporation of additional events and statistics into the analyses.

A fraction of the ^{210}Po located on the AV surface permeates into the fiducial volume, dissolves, and disperses within the scintillator. There, it undergoes alpha decay at a rate of approximately 5% of its activity on the AV surface. In contrast,
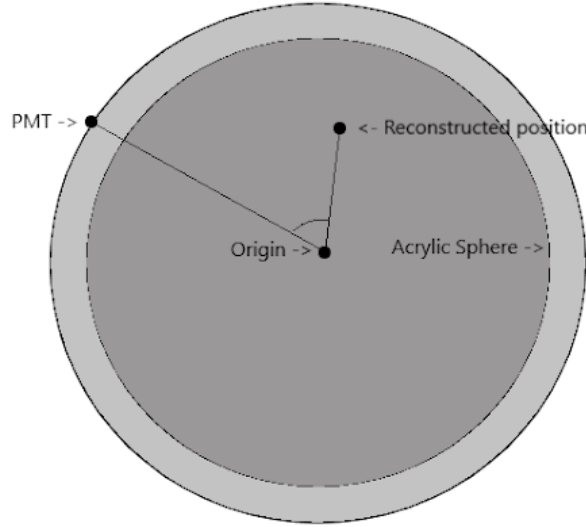
(a) Schematic of a simplified cross section of the detector. Angle used in the position reconstruction algorithm shown here.
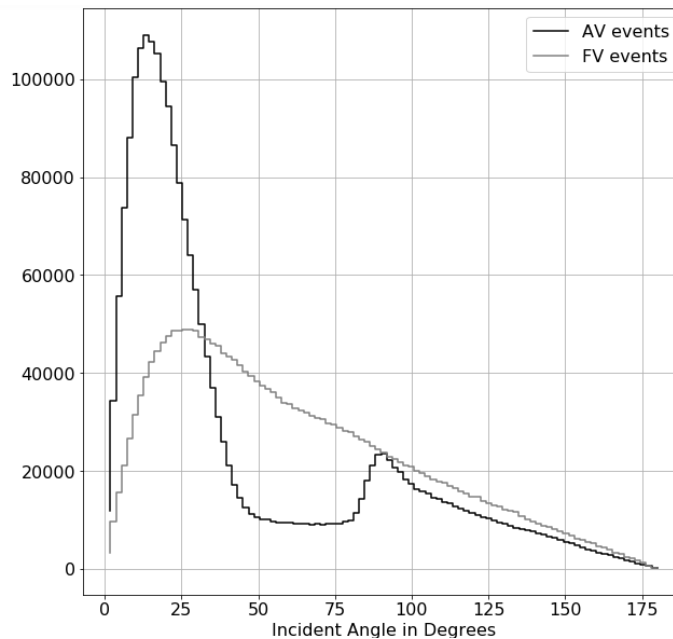
(b) Angular distribution of emitted light for events near/on the acrylic vessel and those occurring deeper within the volume. Events close to the vessel can emit light that strikes the detector at angles equal to or greater than the critical angle. However, light undergoing total internal reflection (TIR) isn't captured by the PMTs, resulting in a noticeable dip in the angular distribution for events near the acrylic vessel.

Figure 4.7: Plots showing the defined angle to be used for the mis-reconstruction detection algorithm and how TIR influences the distribution of angles for different events.

^{210}Bi exhibits lower mobility, with the majority of its activity concentrated on the AV surface. This distinction between ^{210}Po and ^{210}Bi proves useful for observing the effects of misreconstruction from the AV surface into the fiducial volume and for evaluating the method described in later in this chapter, which aims to detect such misreconstructions.

Figure 4.8 illustrates the nhit distribution obtained from recorded data from the scintillator phase of SNO+ at various radial intervals within the fiducial volume. It is evident that, at larger radii within the fiducial volume, the beta decay spectrum of ^{210}Bi events originating from the AV surface becomes observable within the fiducial volume. This phenomenon arises due to the misreconstruction of ^{210}Bi events from the AV surface into the fiducial volume. The high event rate on the AV surface leads to the clouding of event rates in the fiducial volume.

4.4 Mis-reconstructed Position Detection Algorithm

4.4.1 Data

Data in this analysis consisted of:

1. **Simulated**: ^{210}Po events simulated on the AV surface and within FV. These events served as the basis for constructing the probability distribution functions utilized in the likelihood test algorithm employed in this method. Additionally, these events were used to evaluate the performance of the detection algorithm by comparing its output with the known truth data, allowing for the assessment of the detection efficiency for misreconstructed events.

2. **Processed data**: Events obtained from the scintillator phase of the SNO+ experiment. A minimum nhit cut of 70 was applied to investigate the impact of the detection algorithm on ^{210}Po and ^{210}Bi events.
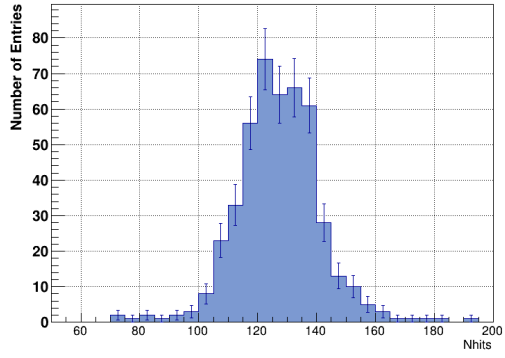
(a) R = (2.14,2.2m)
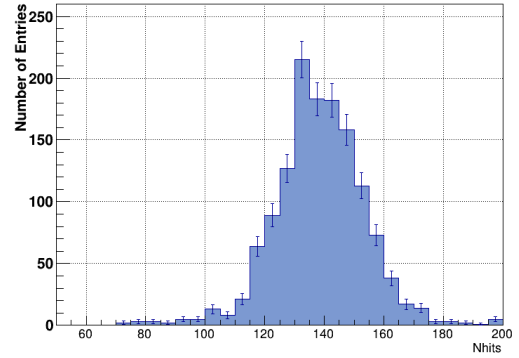
(b) R = (4.04,4.1m)
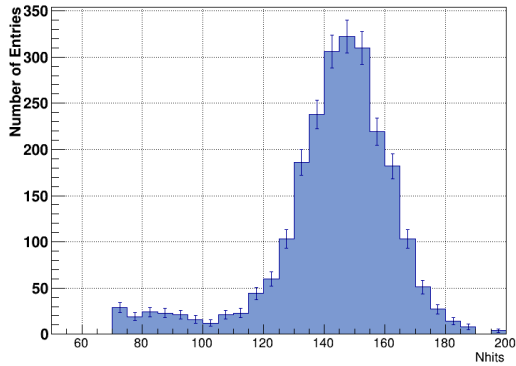
(c) R = (5.14,5.2m)
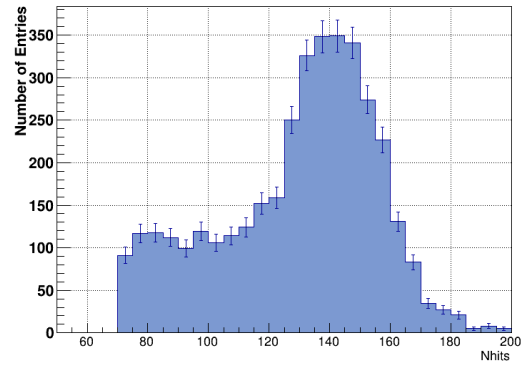
(d) R = (5.39,5.45m)

Figure 4.8: Nhit spectrum for events reconstructed within the FV at various radial cuts and an nhit cut of 70. Bismuth 210 misreconstruction from the AV can be seen at higher radii.

4.4.2 Algorithm

Taking a reconstructed event's fitted position, as determined by the reconstruction algorithm, F and the positions of the PMTs the light from this event triggers, P_i we can define line segments $\overline{FC_i}$ and $\overline{PC_i}$, where the center of the detector is denoted as C. These line segments form "angles of incidence" denoted as a_i.

The distribution of these angles varies depending on the position of an event within the detector. For a given event, the distribution of these angles can be matched to either of the following:

1. A distribution of angles of incidence derived from a substantial number of events simulated on the AV.

2. A distribution of angles of incidence derived from a substantial number of events simulated within the FV.

To match events to one of these distributions a log-likelihood test was used. The distributions show in Figure 4.7b were binned and transformed into probability density functions (PDFs) as shown in Figure 4.9. Subsequently, a log likelihood test can be performed to assess the likelihood of an event belonging to either the FV or the AV. The likelihood metric, denoted as L, is defined as follows:

$$L = \log(\frac{1}{N} \frac{\prod_i l(a_i, FV)}{\prod_i l(a_i, AV)}) \tag{4.7}$$

Here, for each event, the numerator represents the product of the probabilities associated with each angle of incidence using the PDFs constructed from events within the FV, while the denominator represents the product using the PDFs constructed from events on the AV. A positive output from the classifier indicates that the angular distribution of the PMTs hit by an event is more similar to events within the FV. Conversely, a negative output indicates similarity to events on the AV. To normalize the output of the classifier algorithm for events with varying numbers of hits, this product is divided by the number of hits, N.
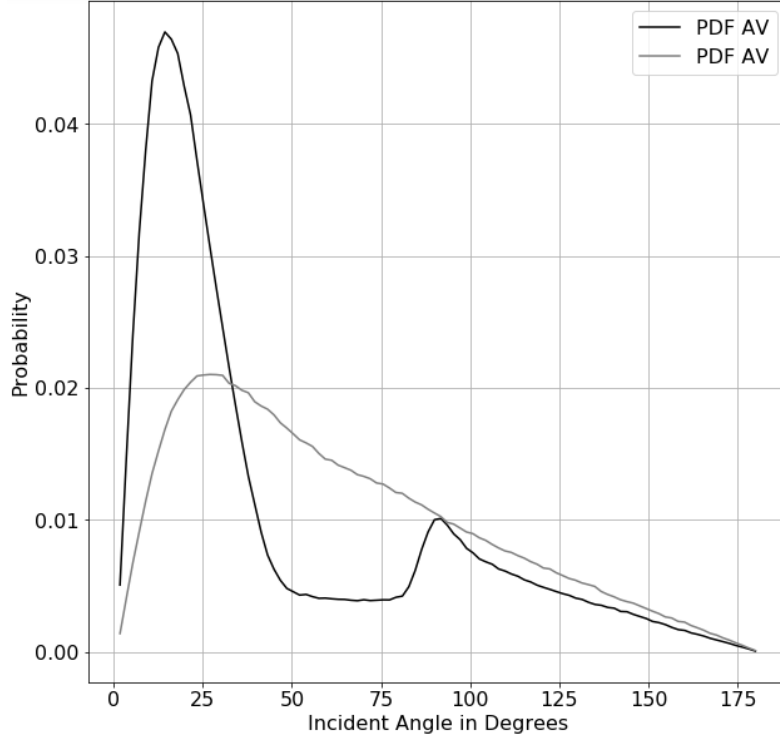
Figure 4.9: Probaility distribution functions that a photon of light emanating from an event strikes the pmt at a particular angle for AV events and FV events

4.4.3 Results

The log likelihood classifier was employed to analyze both simulated and recorded data, as described in Section 4.4.1. The application of this classifier to the data is depicted in Figure 4.10. Specifically, Figure 4.10a illustrates the classifier's performance on simulated events confined within the fiducial volume with a maximum radius of 5.5m, while Figure 4.10b displays its application to events reconstructed within a 5.5m radius using recorded real data. Figure 4.10b reveals a distinct Gaussian distribution centered around a likelihood of approximately -0.3, which is absent in Figure 4.10a, where the events are simulated and the true position is known (as opposed to being reconstructed). This Gaussian distribution can be attributed to mis-reconstructed events that originate on the AV surface but are reconstructed within 5.5m.

The impact of the classifier becomes apparent when examining the energy spectrum plots depicted in Figure 4.8. Figure 4.11 illustrates one of these distributions,

(a) Simulated within 5.5m

(b) Reconstructed from recorded data within 5.5m
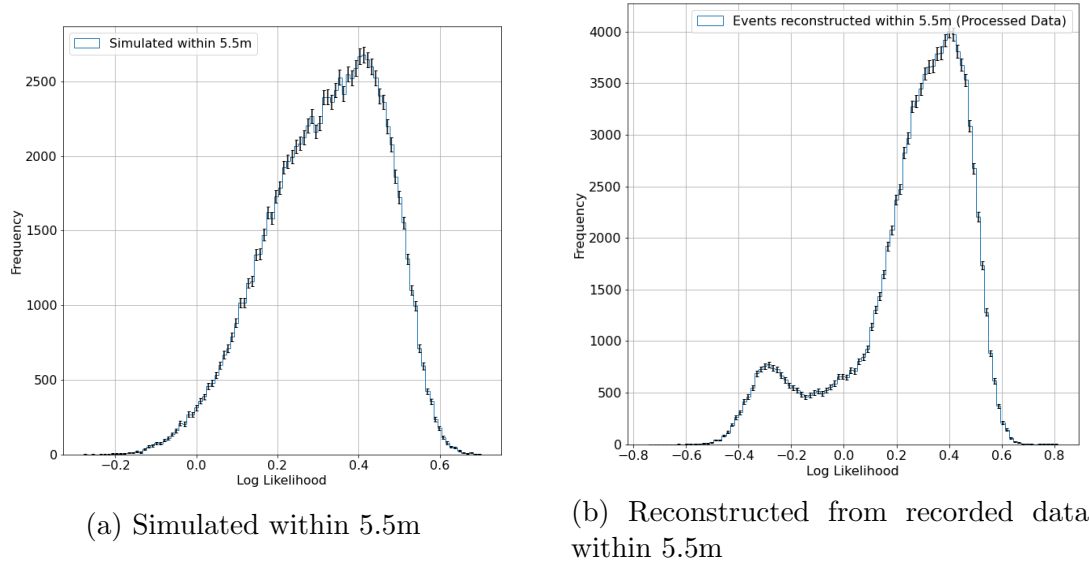
Figure 4.10: Log Likelihood plots of applying the classifier on events simulated in the FV within a radius of 5.5m (a) and events reconstructed from data within a radius of 5.5m (b)

specifically the one bound within R = (5.39, 5.45)m. Prior to implementing the classifier with a log likelihood cut of 0.1, Figure 4.11a exhibits the energy spectrum of ^{210}Bi beta decay events. These events, originating from the AV surface, are improperly reconstructed and do not appear deeper into the fiducial volume. However, upon applying the classifier, as illustrated in Figure 4.11b, the mis-reconstructed events are effectively eliminated, leaving only the ^{210}Po alpha decay spectrum. This resultant energy spectrum closely resembles the spectrum observed at greater depths within the fiducial volume and is what we would expect to see if events were reconstructed ideally.

Results: Identification of Event Mis-Reconstruction into the Fiducial Volume

In order to assess the effectiveness of the classifier in mitigating mis-reconstruction, it is necessary to evaluate its performance on simulated mis-reconstructed events. These events are exclusively simulated on the AV surface, with only those that exhibit

(a) No classifier applied

(b) Classifier applied
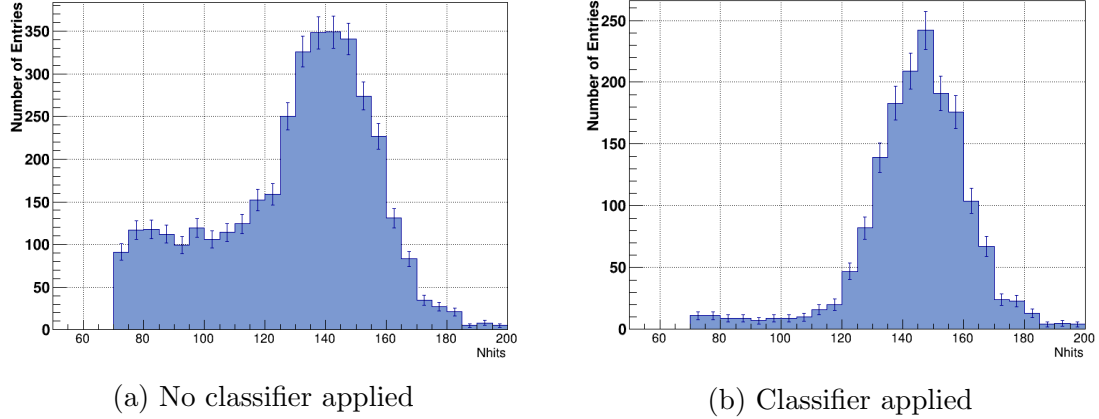
Figure 4.11: Nhit distribution of events reconstructed at a radius of (5.39,5.45)m before and after the application of a log likelihood cut of 0.1. Bismuth mis-reconstruction can be seen removed

mis-reconstruction within the fiducial volume being retained. Figure 4.12 visually presents this simulated mis-reconstruction at various fiducial volume thresholds, both before and after the application of the classifier. A blanket log likelihood cut of 0 is employed for the classifier. By examining the logarithmic plots we can see the extent of mis-reconstruction is notably influenced by the radius. Encouragingly, the classifier demonstrates an ability to eliminate a significant portion of the mis-reconstructed events.

False Positives

An essential aspect to consider when expanding the usable fiducial volume through the implementation of a classifier cut is to assess its impact on events that genuinely lie within the fiducial volume. The impact analysis of the classifier on these events is depicted in Figure 4.13, which illustrates the percentage of events removed in both simulation and recorded data for various radial cuts, while maintaining a log likelihood cut of 0. The observations from the plot can be summarized as follows:

In simulation, the removal of events within a fiducial volume of 5.5m is minimal, with a maximum of 2% of events being affected. This is a negligible loss of events in

38
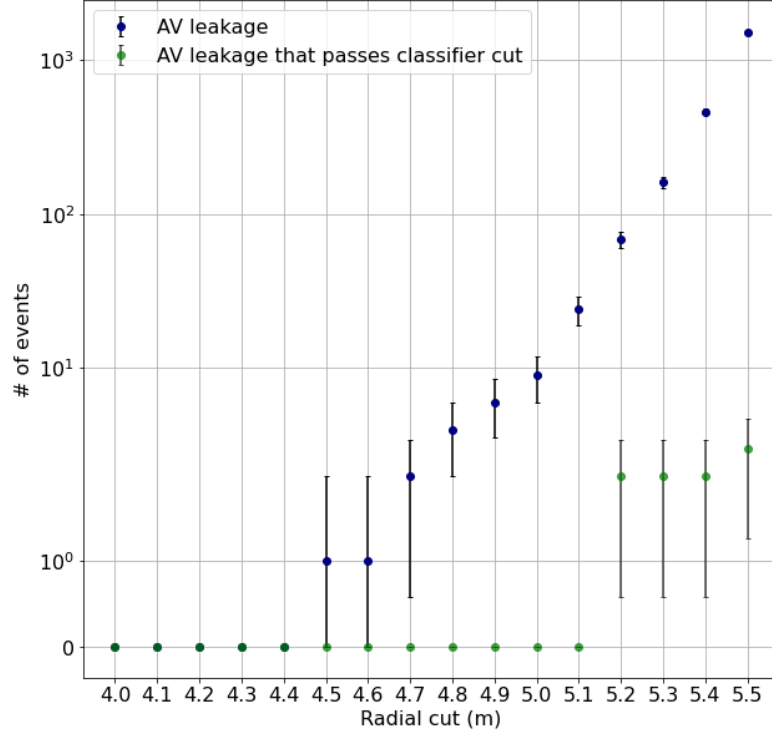
Figure 4.12: Mis-reconstruction into the FV at different radius cuts before and after the application of the classifier

comparison to the potential gain in event rate achievable from utilizing the additional volume.

In recorded data, the removal of reconstructed events within a fiducial volume of 5.5m reaches up to 8%. Nonetheless, this fraction of removed events remains negligible when considering the increase in event rate resulting from the scaling of the volume. Moreover, it is worth noting that these removed events are likely to be significantly contaminated by undesired mis-reconstructed events.

Overall, these findings emphasize the favorable trade-off between the classifier's impact on event removal and the subsequent benefits of expanding the fiducial volume.
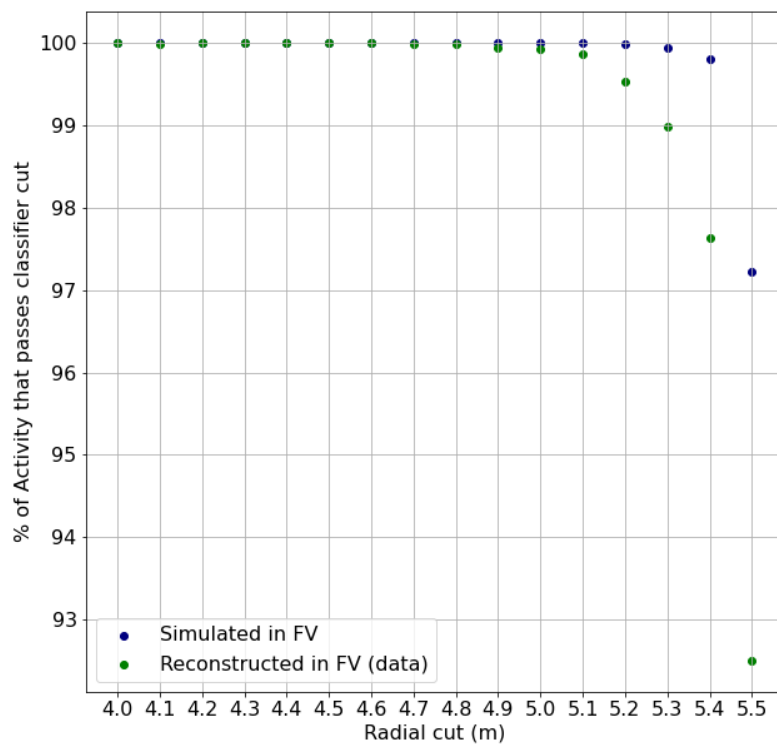
Figure 4.13: Percentage of events that get removed by the classifier that are simulated within the FV at different radii (blue) or reconstructed at different radii from real data (green)

Chapter 5

Movement of Polonium 210:

This section presents an analysis of the influx and dispersal of ^{210}Po within the fiducial volume. Specifically, it focuses on a period of heightened ^{210}Po event rate in distinct sections of the detector during late April and early May 2022. To investigate this phenomenon, the fiducial volume is partitioned into various area sections, and the event rates over time within these sections are examined. The analysis reveals a discernible flow of ^{210}Po along the z-axis from the bottom to the top of the detector. Furthermore, employing the classifier described in Section 4, this flow can be traced up to 10cm from the AV wall, extending to the periphery of the detector.

5.1 Mixing of Polonium 210

The behavior of ^{210}Po within the fiducial volume exhibits distinct phases, transitioning between periods of homogeneous distribution and localized spikes in event rate. Figure 5.1 illustrates the event rate of ^{210}Po at varying radial distances from the detector's center during the timeframe of late April to early May 2022. The x-axis, labeled as $run\#$, represents discrete one-hour intervals of live recording time, with each data point corresponding to the cumulative event rate for that specific run.

In this plot we see radioacative decay of ^{210}Po over the run range (300000, 300750). A notable observation from the figure is the apparent influx of ^{210}Po concentrated within the radial shell encompassing a distance range of 5 to 5.5 meters from the

detector center, occurring around run 300750. The material in this spherical shell can be seen deviating from the general downward trend. Subsequently, this material gradually propagates towards the central spherical shells of the detector over time. This propagation to the center of the detector can be seen peaking at around run 301600 where the spherical shell encompassing a distance range of 0.5 to 1 meters from the detector center can be seen reaching an event rate of ~ 280 events $\frac{\text{events}}{h \cdot m^3}$.
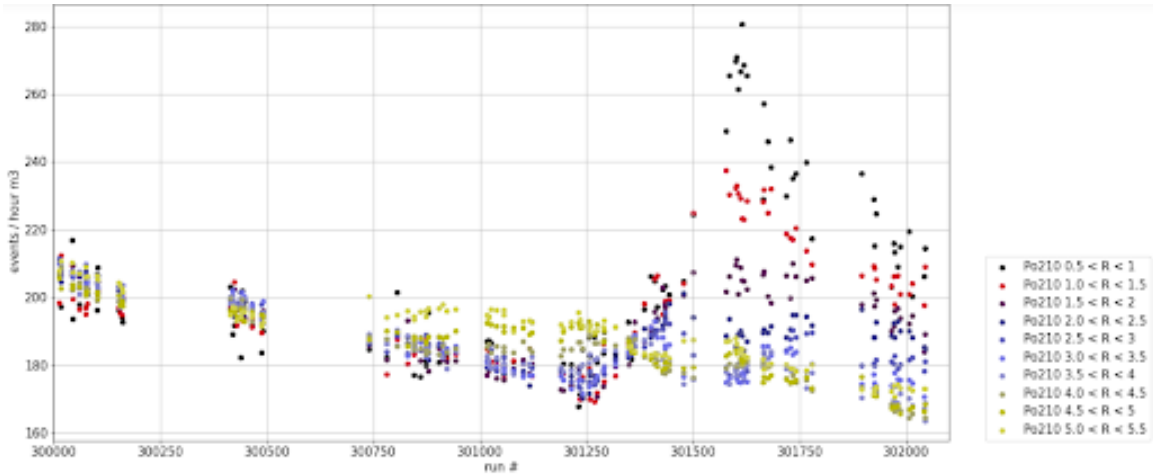
Figure 5.1: Polonium 210 rates at different FV shells over a run period. Influx of material can be seen at the outermost spherical shell at $\sim$ run 300750 disrupting the pattern of homogenous radioactive decay. This material disturbs the general mixed rates across shells and causes the peak seen in the innermost spherical shell at $\sim$ run 301600.

5.2   Dividing the Detector into Cubes

In order to gain preliminary insights into the event rates within distinct regions of the detector, a straightforward approach involving partitioning the detector into cubes was employed. This method provides a convenient means of assessing the event rate variations within localized sections of the detector, enabling the identification of any noteworthy deviations from the expected homogeneous event rate.
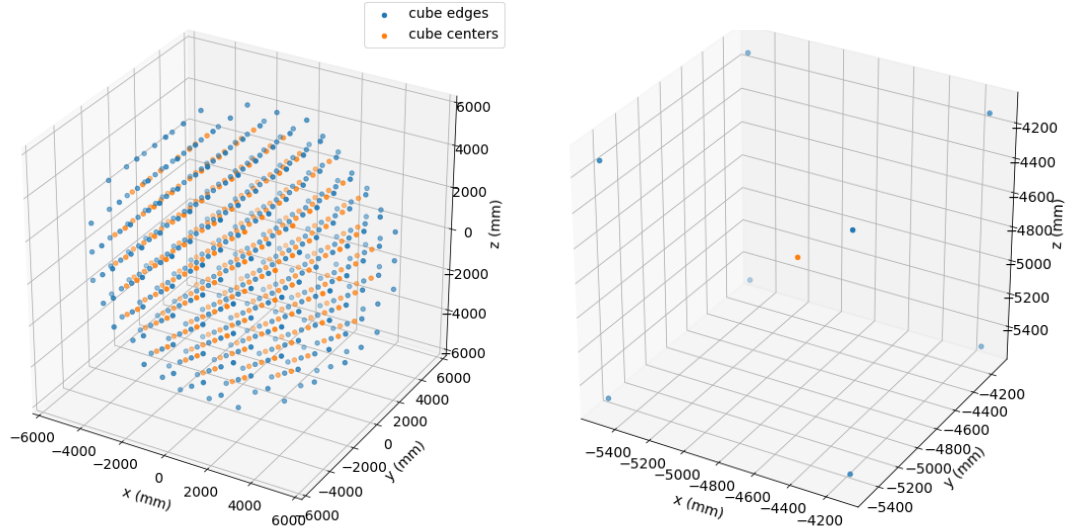
(a) All cubes within 5.5m of the detector center

(b) Example of one cube section

Figure 5.2: Dividing the detector into cubes. Orange is the cube center and blue the cube edges

5.2.1 Method

In order to ensure accurate event rates and eliminate any interference from the AV surface, events located within a distance of 5.5m from the detector center were exclusively considered. By doing so, the event rate within the fiducial volume remains unaffected by misreconstructed events originating elsewhere.

To partition the detector, an large cube with a side length of 5.5m is taken. This cube is then divided into 512 smaller cubes by subdividing each side of the larger cube into eight equal segments. Subsequently, a radial cut of 5.5m from the center of the cube is implemented, resulting in the removal of all cubes located beyond this radial distance.This leaves 280 cubes, as depicted in Figure 5.2. Figure 5.2a illustrates the cube centers and boundaries for all 280 cubes, while Figure 5.2b provides a visual representation of one of these cubes in this partitioning process.

5.2.2 Results: Local rates of Polonium 210 activity

General rates

The run period encompassing $run\#'s$ (301250, 301410) was chosen for analysis, focusing on the inflow of material into the central spherical shells of the detector. Within this timeframe, the event rates within each of the 280 cubes were recorded.

Figure 5.3 displays the event rates of these cubes throughout the run period, albeit with a visually cluttered plot. Nevertheless, it reveals two distinct instances of heightened activity in eight specific cubes. Initially, four cubes exhibit an increasing event rate, reaching its peak around run number 301340. Concurrently, another set of four cubes shows a surge in event rate. Interestingly, this surge coincides with the decrease in event rate observed in the first set of four cubes, indicating a transfer of ^{210}Po activity from the first set to the second set of cubes.
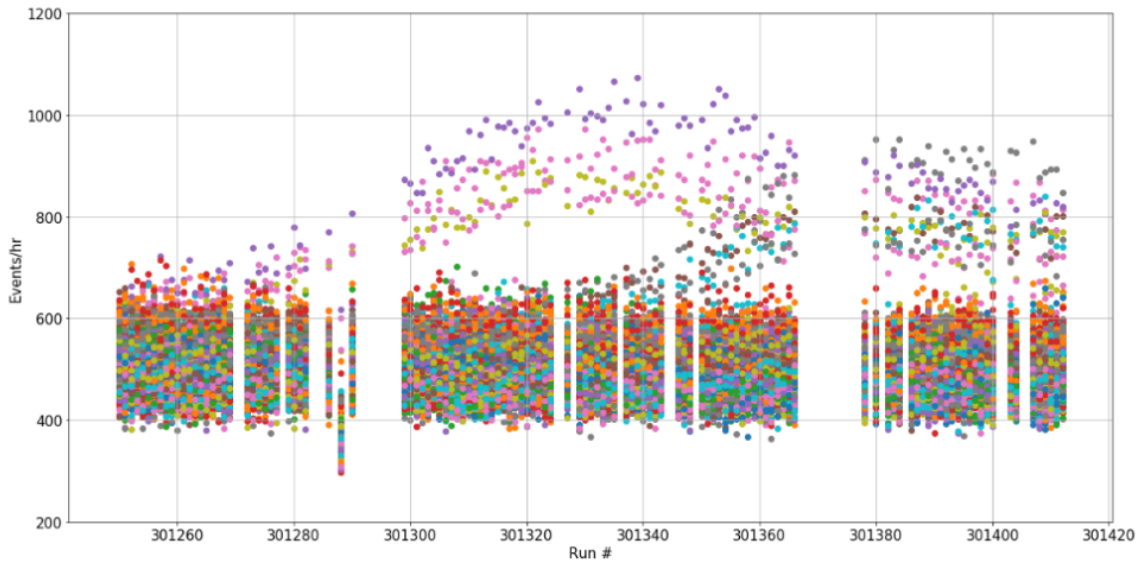
Figure 5.3: Plot illustrating event rates of individual cubes, with each color denoting a different cube. Two distinct regions of heightened activity are observed: at run 301250, four cubes exhibit increasing activity peaking at $\sim$ run 301340, and at around the same run $\sim$ 301340, a subsequent set of 4 cubes begin to display an increase in activity

Areas of interest

We can now take a closer look at these "cubes of interest" and their event rates. Figure 5.4 provides a clearer representation of the two sets of cubes, highlighting their increasing event rates. Figure 5.4a specifically focuses on the first set of cubes, clearly demonstrating the aforementioned trend of an escalating event rate commencing at the beginning of the selected run period. Furthermore, Figure 5.4b displays a similar rising event rate for the second set of cubes, which aligns with the peak and subsequent decline observed in the event rate of the first set of cubes.

The aforementioned sets of cubes lay near the bottom of the detector, in close proximity to the z-axis. Fig. 5.5 visually depicts the precise locations of these two sets. Notably, the initial set of cubes to experience the increase in event rate comprise the four cubes positioned at the lowest extent along the z-direction out of the 280 cubes. Evidently, this influx of material at the detector's base ascends vertically along the z-axis, reaching the second set of cubes situated one layer higher and also aligned with the z-axis. This suggests a discernible material flow originating from the bottom of the detector and traversing towards the origin along the z-axis.

5.3 Flow of Polonium 210 up through the center of the detector

To gain a clearer understanding of the material flow upwards through the detector, we can examine the region around the z-axis more closely. One way to do this is by considering stacked cylinders along the z-axis and observing the event rate within these cylinders over time. This analysis will enable us to identify any changes in the event rate and visualize the material's movement within the detector more effectively.
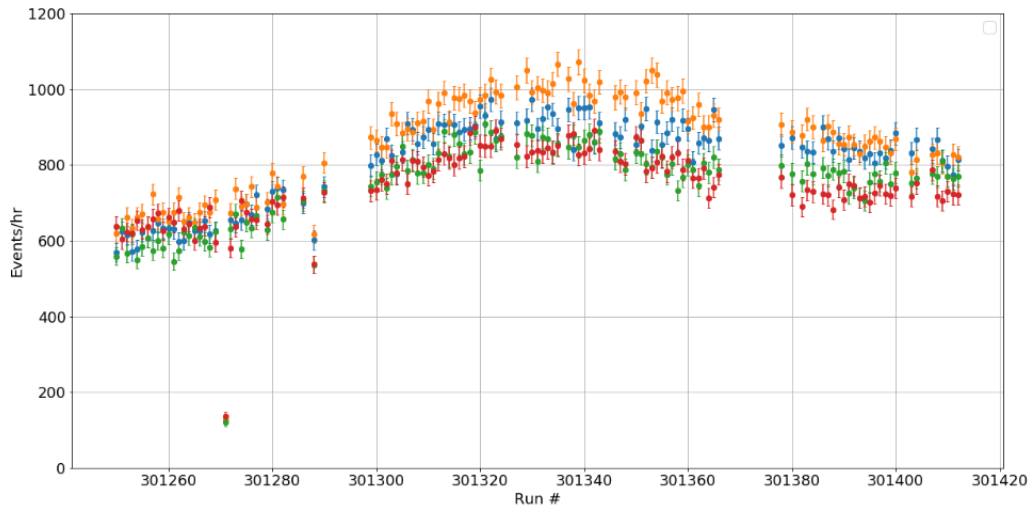
(a) Cubes centered at R ∼ 4.9m and Z ∼ -4.9m
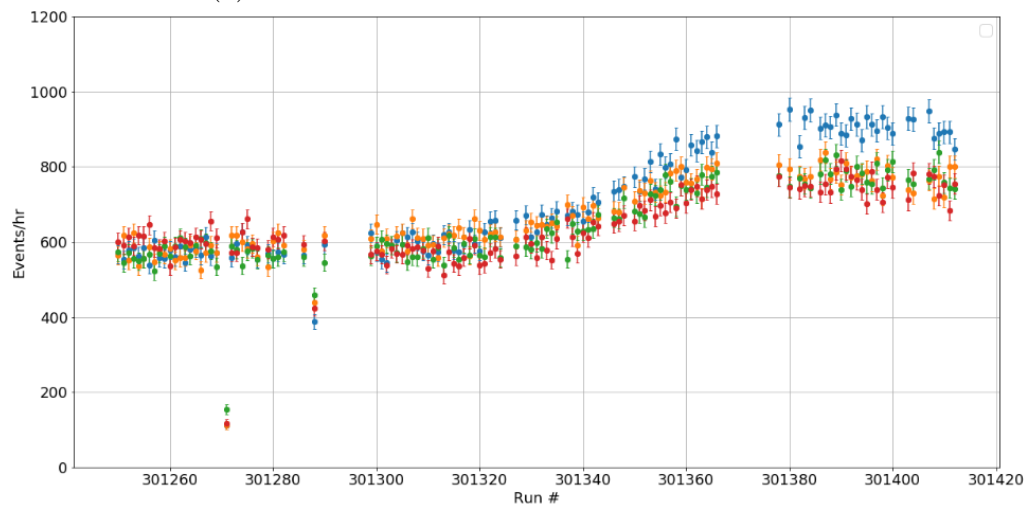
(b) Cubes centered at R ∼ 3.5m and Z ∼ -3.5m

Figure 5.4: Event rates of cubes which shoot off with higher event rates at separate times

5.3.1 Dividing the detector into rings

In order to observe the material flow within the detector, a series of stacked cylinders was employed, aligned along the z-axis and each measuring 200mm in height. The first cylinder originates at a depth of -5.3m in the z-direction, while subsequent cylinders are stacked up to a depth of 5.3m, as depicted in Figure 5.6a. To facilitate the analysis, each cylinder is further subdivided into concentric tubes of varying radii, as illustrated in Figure 5.6b. These tubes divide each cylinder into three distinct regions spanning the ranges (0, 1200 mm), (1200, 1600 mm), and (1600, 2000 mm) in the x-y plane perpendicular to the z-axis. By employing this tube-based segmentation, we can effectively discern the minimal thickness of the material flow current within the detector
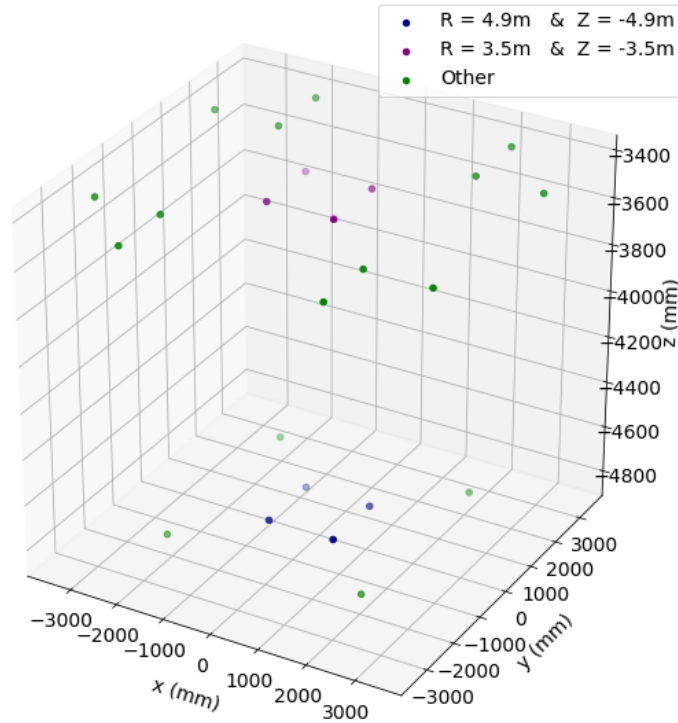
Figure 5.5: Visual of the cubes of interest

47

(a) Schematic of all cylinders stacked on top of each other

(b) Example of one cylinder section
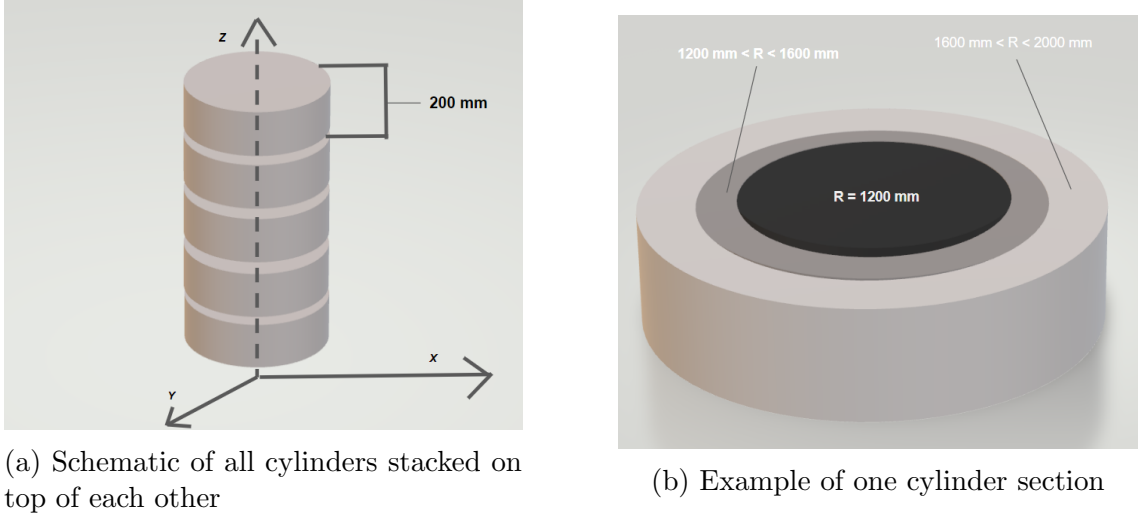
Figure 5.6: Dividing the detector into rings

5.3.2 Results: Moving peaks of Polonium 210 Activity

The investigation now turns to the temporal evolution of event rates within these cylinders. The four plots presented in Figure 5.7 depict the event rate as a function of time for each respective cylinder. Commencing with the first plot, Figure 5.7a, representing the bottommost cylinder spanning the Z range (-5.3, -5.1 mm), we observe an evident influx of material commencing from the initial recorded run, run 301250, and reaching its peak around run 301300. The subsequent plot, Figure 5.7b, corresponding to the cylinder stacked three levels above the bottommost one, exhibits a delayed influx of material in comparison to its lower counterpart, indicating a upward flow from the bottommost cylinder. Analogously, the ensuing plots, Figure 5.7c and Figure 5.7d, representing cylinders positioned successively higher within the detector, manifest a similar pattern of delayed material influx relative to the cylinders beneath them. Consequently, a discernible flow of material ascending through the central region of the detector becomes apparent. It is worth noting that while only a subset of cylinders are depicted herein to illustrate the material flow, all intermediate cylinders exhibit analogous behavior.
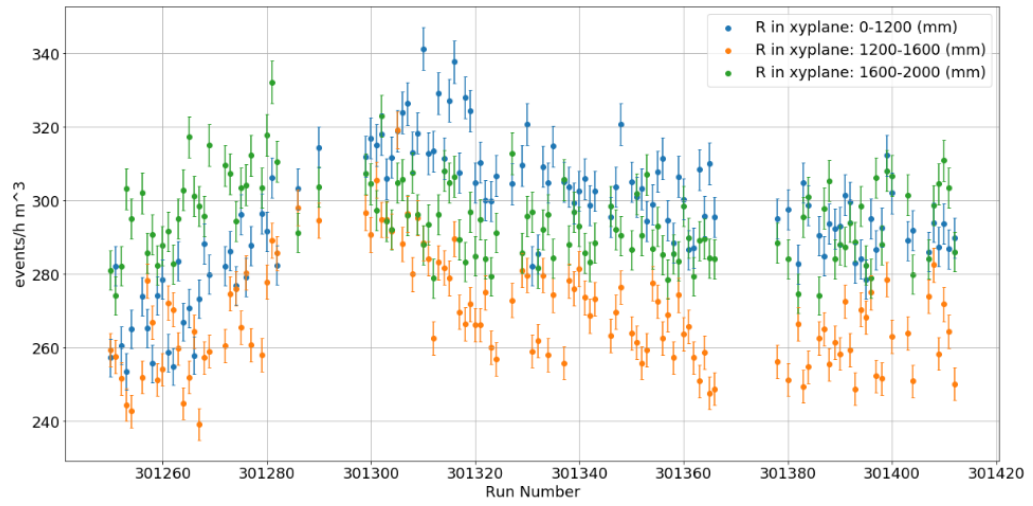
(a) Z =(-5.3,-5.1)m
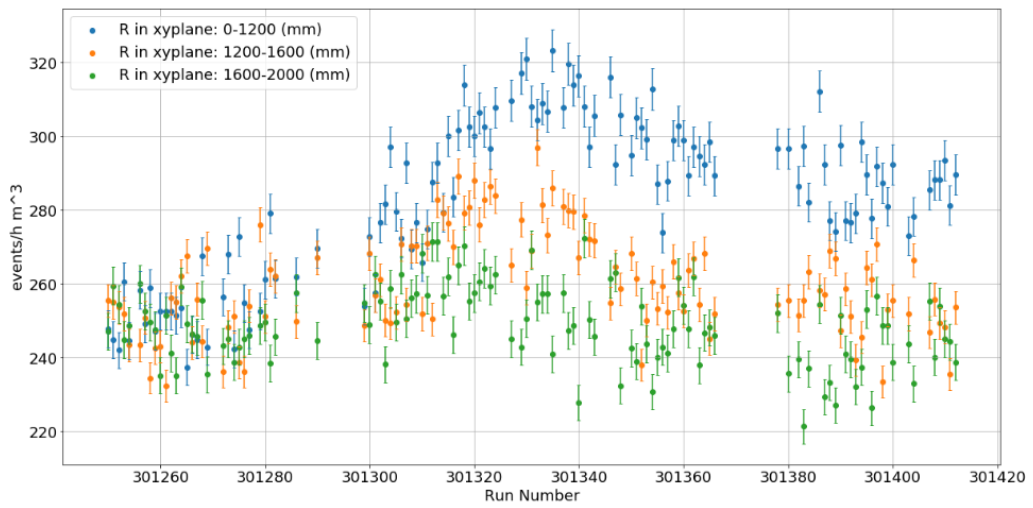
(b) Z =(-4.7,-4.5)m
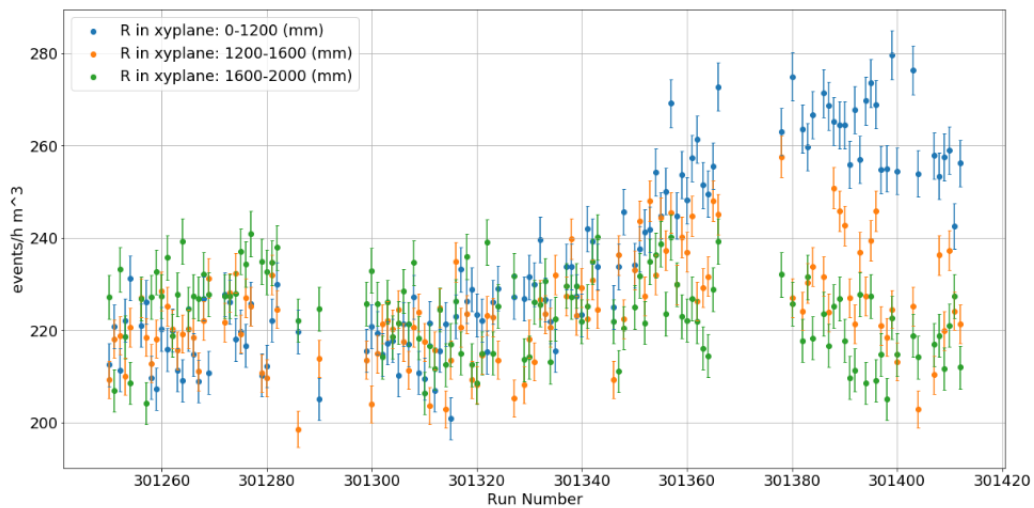
(c) Z =(-3.7,-3.5)m
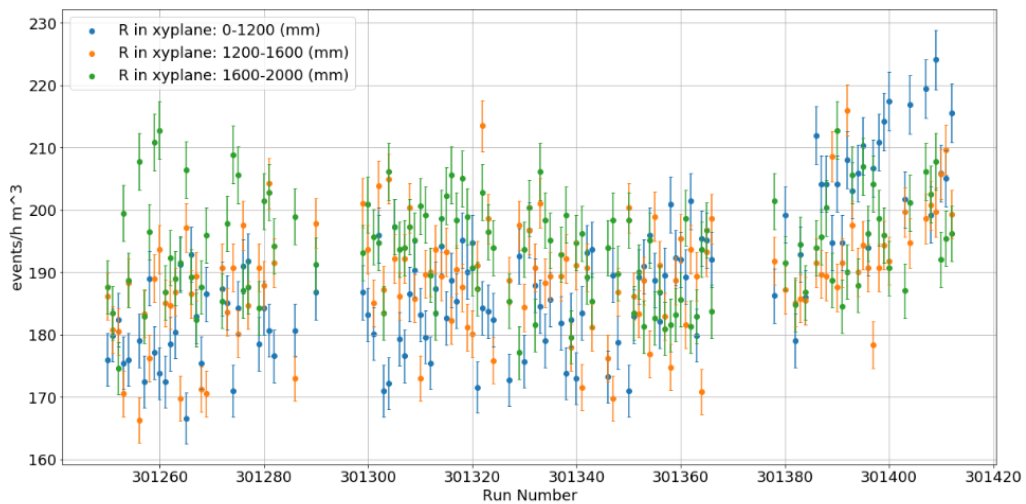
(d) Z =(-2.7,-2.5)m

Figure 5.7: Event rates in different cylinders centered around the z axis with a height of 200mm. Influx of material can be seen rising through the cylinders sequentially

5.3.3 Results: Estimating a flow rate

In this section, we present the estimation of the flow rate of ^{210}Po through the detector. To achieve this, we consider a concentric tube of radius R in each 0.2m thick cylinder section. The selection of the radius R is based on enforcing the condition of a uniform flow through the tube.

To estimate this radius R, radii ranging from 1.20m to 1.60m were chosen in 50mm increments (1.20m, 1.25m, 1.30m... 1.60m). The maximum event rate per unit area over the run period was recorded for each concentric tube. The radius R used was determined as the largest cylinder radius satisfying an event rate within a 5% deviation from that of the 1.20m cylinder. This process can be mathematically expressed as follows:

$$R = \arg\max_{R_i}\{E_i \leq 1.05 \cdot E_{\text{ref}}\} \tag{5.1}$$

where R_i represents the individual cylinder radii, E_i denotes the event rate for each cylinder, and E_{ref} signifies the event rate for the 1.20m reference cylinder. After evaluation, the radius R that satisfies this uniformity condition was found to be 1.350m, defining the cylinder section of interest.

To estimate the flow rate of material influx into a cylinder section, a method employing moving averages was utilized. For each cylinder section, the following steps were carried out:

- Let R_i represent the event rate for each run within a designated run window.

- The runs were examined sequentially, starting from the first run, to identify any increase in event rates.

- A moving average window of 8 runs was employed.

- Sequentially, each run i was paired with the subsequent 7 runs $(i + 1)$ through $(i + 7)$.

- The average event rate across these 8 runs was computed.

- This average event rate was compared to the average event rate observed in the subsequent 8 runs $(i + 8)$ through $(i + 15)$.

- If the event rate for the latter 8 runs was at least 63 events per cubic meter greater than the average event rate of the preceding 8 runs, the first run in the pair, R_i, was considered as the time at which an influx of material enters the system.

- The index i iterates sequentially through the runs, allowing for the identification of the specific run at which the influx of material occurs.

This process can be formally represented by the following logical statement:

If

$$\frac{1}{8} \sum_{j=i}^{i+7} R_j < \frac{1}{8} \sum_{j=i+8}^{i+15} R_j - 63 \tag{5.2}$$

then run i is identified as the run at which the influx of material enters.

This procedure is carried out for 13 cylinder sections. The cylinder sections range from z = (-5.3 m, -5.1 m) to z = (-2.9 m, -2.7 m). Consequently, we obtain a time t_c for each cylinder section, indicating when the material enters that specific section. By subtracting the time t_c at which material enters a cylinder section from the time t_{c-1} at which it enters the cylinder section below, we calculate 12 time differences. These time differences serve as 12 separate estimates of the flow rate of the material influx through the detector.

The mean of these time differences is found to be 10.2 hours, with a standard deviation of 1.8 hours. Consequently, the volume flow rate is calculated as:

$$\frac{V}{t} = \frac{\pi (1.35^2 \, \mathrm{m}^2)(0.2 \, \mathrm{m})}{10.2 \, \mathrm{h}} = 0.11 \pm 0.019 \, \frac{\mathrm{m}^3}{\mathrm{h}} \tag{5.3}$$

Furthermore, to investigate the impact of variations in the geometry of the concentric tube on the flow rate estimation, we repeated the measurements using two

different configurations.

Firstly, we utilized a concentric tube with a reduced radius of 0.8 meters instead of 1.2 meters. The flow time for this configuration was measured to be 8.2 hours, with a standard deviation of 4.5 hours. Calculating a flow rate from this gives us:

$$\frac{V}{t} = \frac{\pi(0.8^2 \,\mathrm{m}^2)(0.2\,\mathrm{m})}{8.2\,\mathrm{h}} = 0.049 \pm 0.027\,\frac{\mathrm{m}^3}{\mathrm{h}} \tag{5.4}$$

This flow rate is through an area that is 2.8 times smaller, so an event rate difference of 23 was used as a cut off instead of 63. Adjusting the flow rate here to compare with the concentric tube of radius 1.35m meters gives us a flow rate of: $0.14 \pm 0.0756\,\frac{\mathrm{m}^3}{\mathrm{h}}$.

Next, we maintained the radius of 1.2 meters but reduced the height of the tube to 0.1 meters instead of 0.2 meters. This alternative configuration resulted in a flow time of 7.0 hours, with a standard deviation of 6.3 hours. Calculating a flow rate from this gives us:

$$\frac{V}{t} = \frac{\pi(1.2^2 \,\mathrm{m}^2)(0.1\,\mathrm{m})}{7.0\,\mathrm{h}} = 0.065 \pm 0.0585\,\frac{\mathrm{m}^3}{\mathrm{h}} \tag{5.5}$$

Comparing these new flow rates with the original estimation of $0.11 \pm 0.019\,\frac{\mathrm{m}^3}{\mathrm{h}}$, we observe that the variations in the concentric tube geometry led to varying estimates of flow rates with larger error intervals. These differences suggest that the geometry of the concentric tube can indeed impact the estimated flow rate, and that the errors on the flow rate of $0.11 \pm 0.019\,\frac{\mathrm{m}^3}{\mathrm{h}}$ are under-estimated.

5.3.4 Results: Following the Polonium 210 influx source using Mis-reconstructed Position Detection Algorithm

To trace the origin of this material, our focus shifts to following the flow beyond the depth of z = -5.3m. However, events occurring beyond this point are significantly hindered by misreconstruction of events on Acrylic Surface. In order to examine if the material flow extends closer to the Acrylic vessel surface, we can employ the Mis-reconstructed Position Detection Algorithm outlined in Chapter 4. By utilizing this

algorithm, we can investigate whether the flow extends downwards, reaching closer proximity to the Acrylic vessel surface.

Figure 5.8 showcases the log likelihood distributions of events, ordered from right to left, encompassing the following categories:

- Events simulated within the fiducial volume within a radial range $5.7m \leq R \leq 5.8m$ (orange).

- Events simulated within the fiducial volume within a radial range $5.8m \leq R \leq 5.9m$ (blue).

- Events simulated at a radial distance greater than 5.95m that reconstruct within the range $5.8m \leq R \leq 5.9, m$ (green).

- Events simulated at a radial distance greater than 5.95m that reconstruct within the range $5.8m \leq R \leq 5.9m$ (red).

- Events simulated at a radial distance greater than 5.95m that reconstruct within the range $5.7m \leq R \leq 5.8m$ (purple).

Importantly, all events occurring beyond a radial distance of 5.95m, regardless of whether they reconstruct in that region or not, exhibit a almost identical log likelihood distribution that is shifted to the left relative to events simulated closer to the origin. By implementing a cut value of -0.1 on the log likelihood using this classification method, we can effectively eliminate the majority of events that are misreconstructed in the region proximate to the Acrylic surface, yet still lie within the fiducial volume at a radial distance less than 5.9m. This approach enables us to closely track the material flow observed at z = -5.3m in proximity to the Acrylic vessel surface.

Upon implementing the log likelihood cut, the remaining material predominantly originates within the regions where they reconstruct. To track the flow seen in 5.3.2 two specific regions were examined, defined as follows:

- **Region 1**: The area bounded by a radial range of 5.8m $\leq R \leq$ 5.9m and a depth range of -5.9m $\leq Z \leq -5.8$m.

- **Region 2**: The area enclosed by a radial range of 5.7m $\leq R \leq$ 5.8m and a depth range of -5.8m $\leq Z \leq -5.7$m.

The resulting bounded regions resemble stacked spherical caps located at the bottom of the detector. Figure 5.9 illustrates the event rate within these two regions both before and after the application of the log likelihood cut.

After implementing the log likelihood cut (see Figures 5.9b and 5.9d), we observe a distinct influx of material that closely aligns with the observations made when examining the stacked cylinders in closer proximity to the origin (see Subsection 5.3.2). In both Region 1 and Region 2, the influx of material becomes noticeable starting from run 301200, preceding the observations made in the stacked cylinders closer to the origin, thus supporting the hypothesis that this flow of material is ascending within the detector.
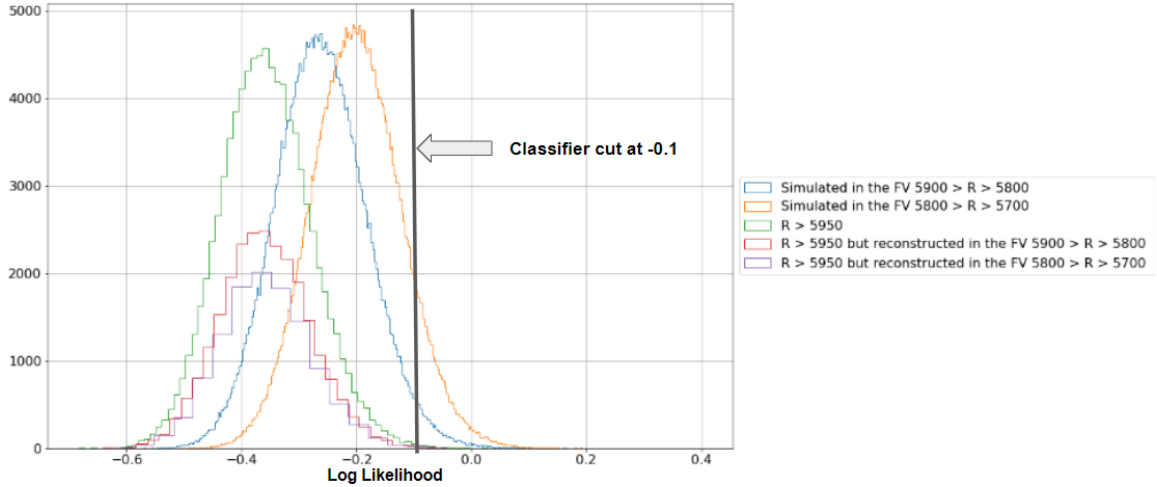
Figure 5.8: Log Likelihood distributions of events simulated near to and on the Acrylic surface
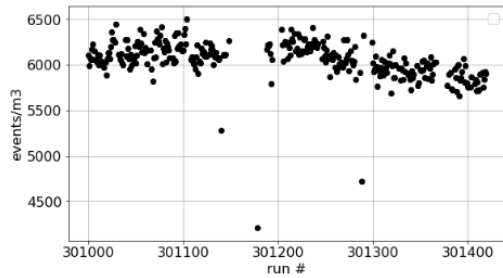
(a) R = (5.8 , 5.9)m & Z = (-5.9 , -5.8)m classifier not applied
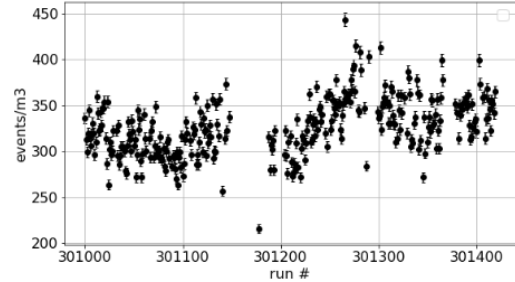
(b) R = (5.8 , 5.9)m & Z = (-5.9 ,-5.8)m classifier applied
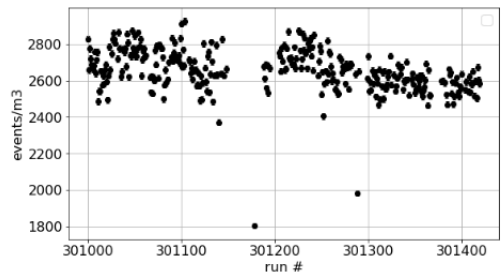
(c) R = (5.7 , 5.8)m & Z = (-5.8 , -5.7)m classifier not applied
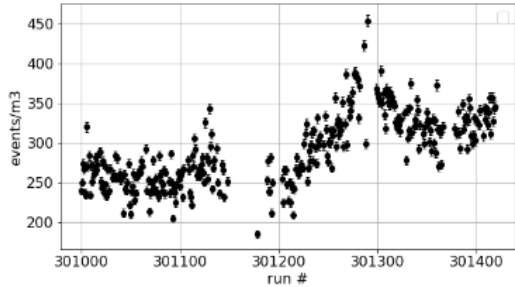
(d) R = (5.7 , 5.8)m & Z = (-5.8 , -5.7)m classifier applied

Figure 5.9: Event rates of sections at the bottom of the detector before and after the classifier is applied near the AV. The same flow pattern of material moving up the detector can be seen when the classifier is applied

5.3.5 Discussion on compatible flow patterns seen in simulation

The simulation described in this section was conducted by Dr. John D. Wilson, a member of the SNO+ collaboration and a Professor at the Univeristy of Alberta, who provided me with the necessary simulation details.

In Dr. Wilson's simulations, he utilized the OpenFOAM software to perform a 3D time-dependent simulation of the complete Acrylic Vessel (AV) in the SNO+ experiment. The simulation started with an isothermal initial state, and a lower hemisphere wall cooling strategy was employed by applying a heat flux of -1 $\frac{W}{m^2}$, estimated to be of the right order of magnitude to what is expected in the detector.

The simulation was divided into two parts. In the first portion, which lasted for 6 hours, a standard mesh consisting of 661,536 cells and three wall layers was used. After 6 hours, the fields obtained from this stage were mapped onto a finer mesh with 1,003,934 cells and seven wall layers. This mapping was then continued until reaching a time of t = 12 hours.

Upon analyzing the wall boundary layer at z = -5 m on y = 0 at t = 12 hours, he observed that the coolest region was situated in the outermost four layers of the AV wall, which were sinking. His calculations indicated that the volume flux in the wall boundary layer per unit azimuthal distance was approximately $22 \frac{mm^2}{s}$. To further investigate the flow characteristics, the circumference of the arc at z = -3 m was measured and found to be approximately 32.6 m.

Using these measurements, he estimated the descending volume flux in the wall layer to be around 720 $\frac{cm^3}{s}$. By projecting this flux vertically, taking into account a scaling factor of $[1-(\frac{z}{R})](\frac{1}{2})$, he determined that approximately 625 cm^3/s of potential upwelling was available along the AV axis.

Based on these findings, it was concluded that there existed a volumetric flux of approximately $600\frac{cm^3}{s}$, which could potentially serve as a source for the observed upwelling.

To summarize, the performed simulation involved forced flow induced by cooling the bottom layer of the detector. This resulted in material flowing down a few centimeters off the AV surface, which is not visible in real data due to its proximity to the AV. The downward flow ultimately reached the bottom of the detector.

The estimated volumetric flux of $600\frac{cm^3}{s}$ is 19 times higher than the observed flow rate of $0.11\ \frac{m^3}{h} = 31\ \frac{cm^3}{s}$. While this discrepancy is significant, it can be attributed to differences in the actual heat flux within the detector which is unknown.

This simulation provides a possible explanation for the presence of excess ^{210}Po material in recorded data at the bottom of the detector.

Chapter 6

An Estimate of the total Polonium and Bismuth 210 rates at SNO+:

Determining event rates for different elements can be challenging when their energy spectra overlap. In Figure 4.1, the energy spectra of ^{210}Po and ^{210}Bi are shown to overlap, requiring their separation to obtain individual event rates. This chapter will outline a simulation that models the energy spectrum of ^{210}Bi. Afterwards, the theoretical energy spectrum will be compared to the observed spectrum in the detector. However, due to statistical fluctuations and losses in light transmission within the detector, the theoretical spectrum does not precisely match the measured spectrum. To address this, the theoretical spectrum will be adjusted to better align with the measured spectrum using Gaussian smearing. By following this procedure, the rates of ^{210}Po and ^{210}Bi can be separated, allowing for the demonstration of their temporal evolution in event rate.

6.1   Simulating Theoretical Beta Decay Spectrum

The code utilized to simulate the Theoretical Beta Decay Spectrum is taken from [35]. The algorithm calculates the energy spectrum of the emitted particles in beta decay. More precisely:

- Input Parameters: The code takes several input parameters such as the branch endpoint energy, the number of protons in the daughter nucleus, and the for-

biddenness of the decay. These parameters define the specific characteristics of the beta decay process under investigation. The package uses ENSDF (Evaluated Nuclear Structure Data) files for these input parameters and the specific parameters for ^{210}Bi are taken from [32]

- Fermi Function Approximation: The code applies the Fermi function approximation, which describes the probability distribution of the decay products as a function of their energy. This approximation accounts for the Coulomb interaction between the emitted particle and the daughter nucleus.

- Energy Calculation: The code calculates the energy of the emitted particles or neutrinos based on the chosen decay process and the input parameters. It takes into account the mass difference between the parent and daughter nuclei, the momentum of the emitted particle, and the neutrino mass, if applicable.

- Probability Distribution: Using the Fermi function approximation, the code determines the probability of finding the emitted particle with a specific energy. The probability distribution is obtained by integrating over the energy range of interest, considering the Fermi function and other relevant factors.

- Energy Spectrum: By iterating over a range of energies, the code generates the energy spectrum of the emitted particles. It calculates the probability at each energy point, resulting in a spectrum that represents the likelihood of observing particles with different energies.

Figure 6.1 shows the Beta Decay spectrum of ^{210}Bi produced.

6.2 Gaussian smearing

Theoretical expectations dictate that in an alpha decay, such as that of ^{210}Po, the decay energy should yield a single distinct energy output, thereby resulting in a corresponding singular recorded energy in the detected spectrum. However, practical
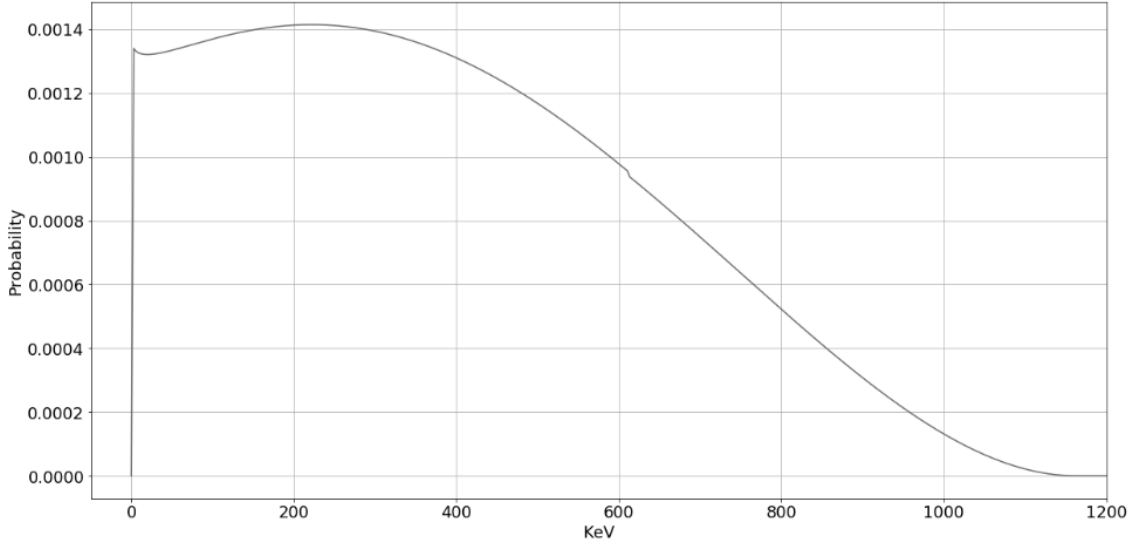
Figure 6.1: Theoretical bismuth decay energy spectrum illustrating the probability of observing various energy levels in a bismuth beta decay. Only the energy of beta particles, an electron here, can be observed as neutrinos do not interact with the scintillator to produce light. The displayed energy values represent the kinetic energy of the emitted electron beta particle, which varies due to the distribution of energy among the electron and the neutrino decay products.

observations, as evidenced by various plots (see Fig. 4.8), reveal that this is not the case. The detected spectrum deviates from the ideal scenario due to statistical fluctuations, imperfections in the detection process within the real-world setup, and losses in light transmission within the detector. Consequently, the measured spectrum exhibits a Gaussian-like distribution.

These statistical fluctuations also exert an influence on the energy spectrum of ^{210}Bi. As depicted in Figure 6.2, the theoretical energy spectrum of ^{210}Bi, when superimposed over the observed spectrum, reveals numerous unaccounted-for events in the $350 >$ nhit >250 range. Within this range, the majority of events are expected to originate from ^{210}Bi decay, as no other isotope or element can explain the observed quantity of events in this specific region. In order to reconcile the measured energy spectrum with that of ^{210}Bi, it is necessary to convolve, or smear, the energy spectrum.

In the regime of nhit > 350, representing energies $>\sim 1$ MeV, a multitude of

higher energy decays become predominant in shaping the energy spectrum. Notably, the energy spectrum within this range is primarily influenced by the decays of ^{214}Bi originating from the scintillator (FV) and acrylic vessel, as well as the presence of ^{40}K and ^{208}Tl on the acrylic vessel, hold up ropes, and within the scintillator. These higher energy decays are not relevant to any of the analyses in this thesis and as such we will ignore them in this section.
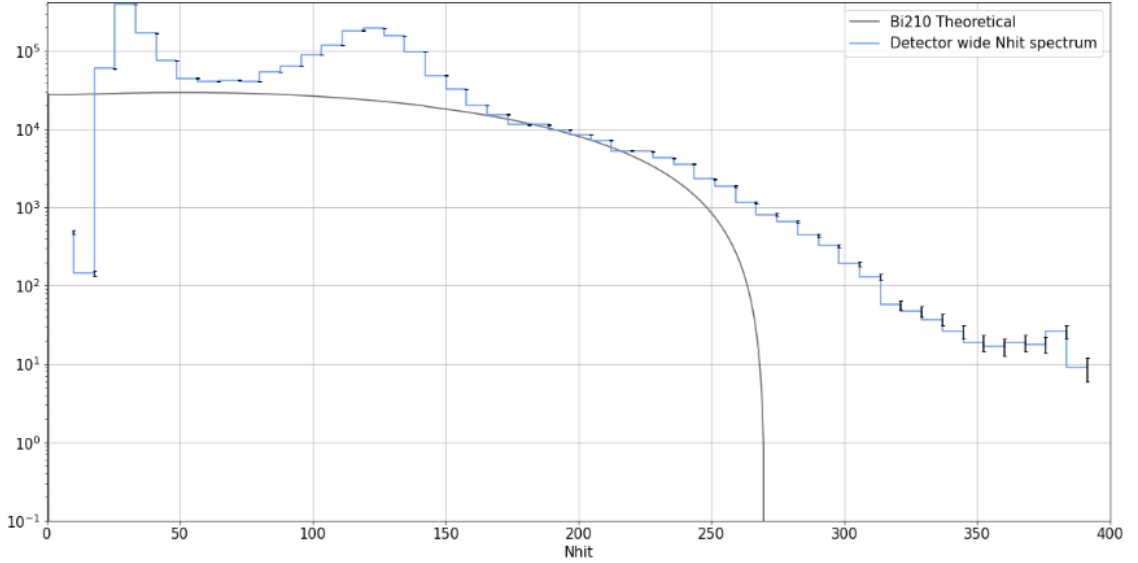
Figure 6.2: Theoretical Bismuth decay energy spectrum overlayed on the Nhit spectrum across the detector

6.2.1 Method

The smeared probability $S_{\text{sm}}(E_i)$ of detecting a specific energy output E_i can be described by integrating the theoretical energy spectrum the range $(0, 500)$. This can be mathematically expressed as a convolution:

$$S_{\text{sm}}(E_i) = \int_0^{500} \frac{1}{\sigma_{E_i}\sqrt{2\pi}} e^{\frac{(E_i - E_{\text{sm}})^2}{2\sigma_{E_i}^2}} S_{\text{interp}}(E_{\text{sm}}), dE_{\text{sm}} \tag{6.1}$$

Where the symbols used in the equation have the following meanings:

- S_{interp} represents the interpolated theoretical energy spectrum, which provides an estimation of the probability value at any given energy.

- E_i corresponds to the specific energy output that undergoes the smearing process.

- The term $\frac{1}{\sigma_{E_i}\sqrt{2\pi}}e^{\frac{(E_i - E_{\text{sm}})^2}{2\sigma_{E_i}^2}}$ represents a Gaussian distribution utilized to smear the theoretical energy spectrum. This distribution accounts for the statistical behavior of the energy values being smeared.

- σ_{E_i} signifies the standard deviation of the Gaussian distribution for the energy E_i. It is calculated as $\sqrt{E_i} \times \sigma$, where σ denotes the standard deviation parameter for the Gaussian distribution. The use of σ_{E_i} instead of a fixed σ ensures that the smearing effect varies with the energy level being considered, capturing the energy dependence of the deviation.

- E_{sm} represents a variable used within the smearing process. Integration of this variable over the range (0, 500) incorporates the contributions from all energy values detected as E_i, accounting for both statistical and real-world imperfections.

Applying smearing process above to a;; E_i described above leads to a modified energy spectrum, exhibiting slight deviations from the original distribution. A visual comparison between the two spectra is depicted in Figure 6.3.

6.2.2 Results: Matching the Bismuth 210 energy spectrum

By superimposing the smeared energy spectrum onto the energy spectrum observed in the detector, we achieve a more accurate approximation of the measured energy distribution. Figure 6.4 presents the nhit spectrum obtained from the detector, with both the theoretical energy spectrum and the smeared energy spectrum overlaid.
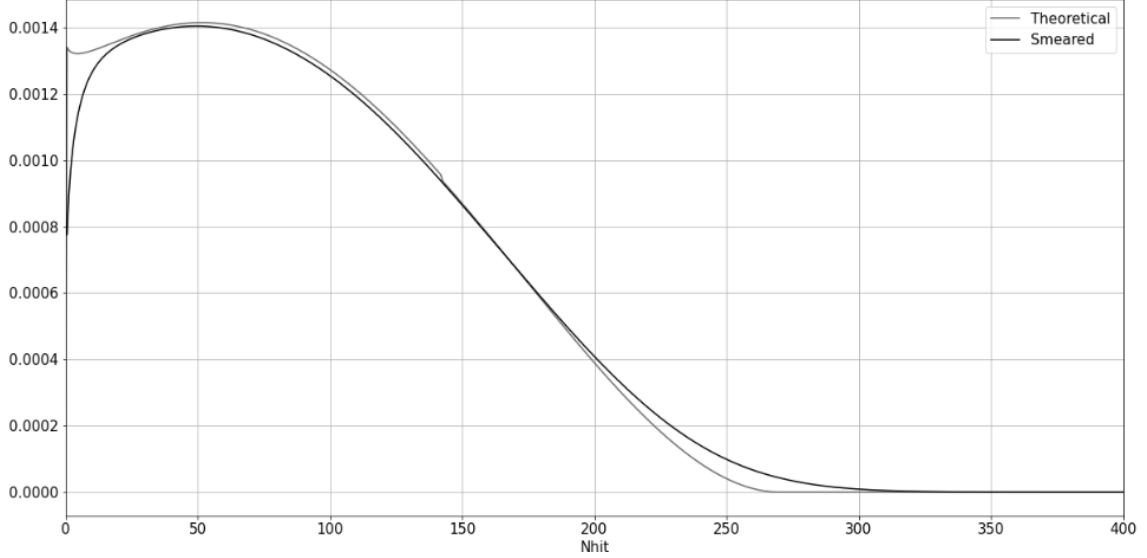
Figure 6.3: Theoretical Bismuth decay energy spectrum vs Gaussian Smeared Bismuth decay energy spectrum

Through iterative experimentation and adjustment of the parameter σ, we can fine-tune the smearing process. As a result, we observe a significantly improved match between the smeared spectrum and the measured spectrum, particularly for events with 350 > nhit > 250. This refined matching demonstrates the effectiveness of the smearing technique in reproducing the energy distribution more closely.

6.3 Splitting the nhit spectrum into individual sources

The smeared energy spectrum obtained can now be utilized to extract the event rates of ^{210}Bi and ^{210}Po from the nhit distribution. In the following, we describe the method employed to accomplish this task, which is subsequently applied to multiple consecutive runs to obtain an estimation of the background event rates.

6.3.1 Method

In a given run, the splitting process can be described as follows:

- Initially, the smeared energy spectrum is compared to the observed spectrum within the energy range of 200 nhits< E < 320 nhits, where primarily ^{210}Bi

events occur. The total number of measured events, denoted as N, within this range is calculated. Furthermore, the probability of a ^{210}Bi event registering within the energy range of 200 nhits $<$ E $<$ 320 nhits, denoted as $P_{>200}$, is determined by summing the contributions from the smeared energy spectrum within that range.

- To align the simulated spectrum with the observed spectrum, a scaling factor is determined by fitting the smeared energy spectrum to the events we see at an nhit range 200 nhits$<$ E $<$ 320 nhits. This scaling factor, denoted as $\frac{N}{P_{>200}}$, represents the ratio between the total measured events N and the probability $P_{>200}$.

- The obtained scaling factor is then multiplied and summed throughout the entire smeared energy spectrum, resulting in a total projected ^{210}Bi event rate, denoted as $N_{\mathrm{Bi}} = \sum_{E_i} S_{\mathrm{sm}}(E_i)$, where N_{Bi} represents the total number of bismuth events.
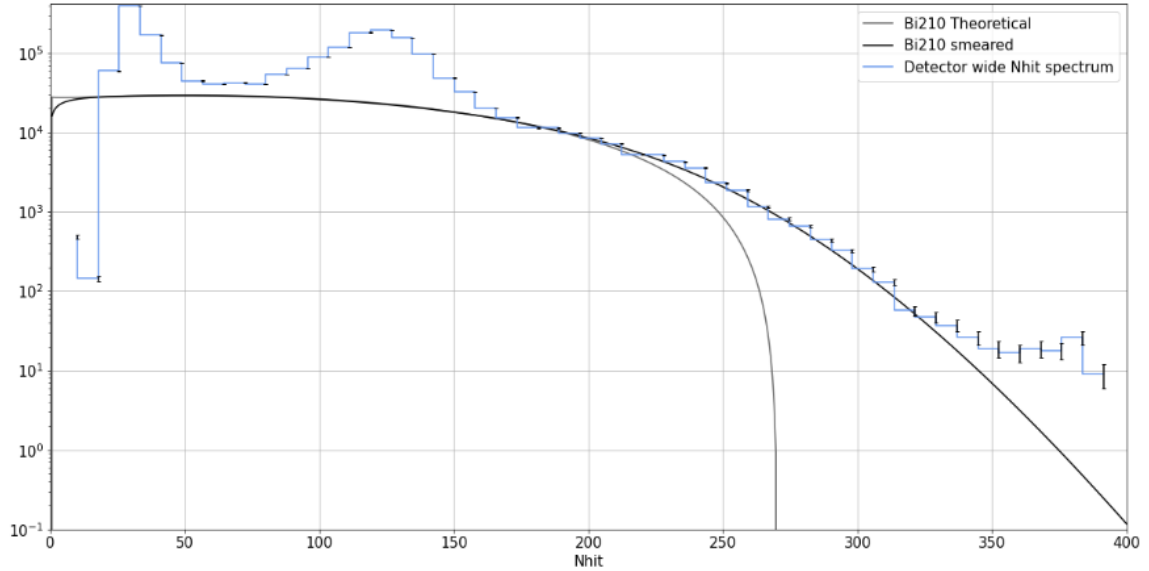
Figure 6.4: Gaussian Smeared Bismuth decay energy spectrum overlayed on the Nhit spectrum across the detector

- Subsequently, in regions where ^{210}Po and ^{210}Bi spectra overlap, the total recorded event rate is subtracted from the projected ^{210}Bi event rate within that region, yielding the projected ^{210}Po event rate.

Figure 6.5 illustrates the outcome of the splitting procedure, showcasing the successful isolation of projected ^{210}Bi (depicted in blue) from the overall energy spectrum (depicted in black). Consequently, two distinct Gaussian distributions emerge in purple, representing ^{14}C and ^{210}Po, respectively. The left Gaussian distribution within the nhit range (25,55) corresponds to ^{14}C events, while the right Gaussian distribution within the nhit range (60,160) corresponds to ^{210}Po events. The particularly wide nhit range for Polonium is attributed to the presence of events on the AV as well as events in the FV, which undergo varying degrees of attenuation at different depths, resulting in a broad range of possible nhit values. The separation of ^{14}C and ^{210}Po events can be achieved by implementing a simple nhit cut between the two distributions.
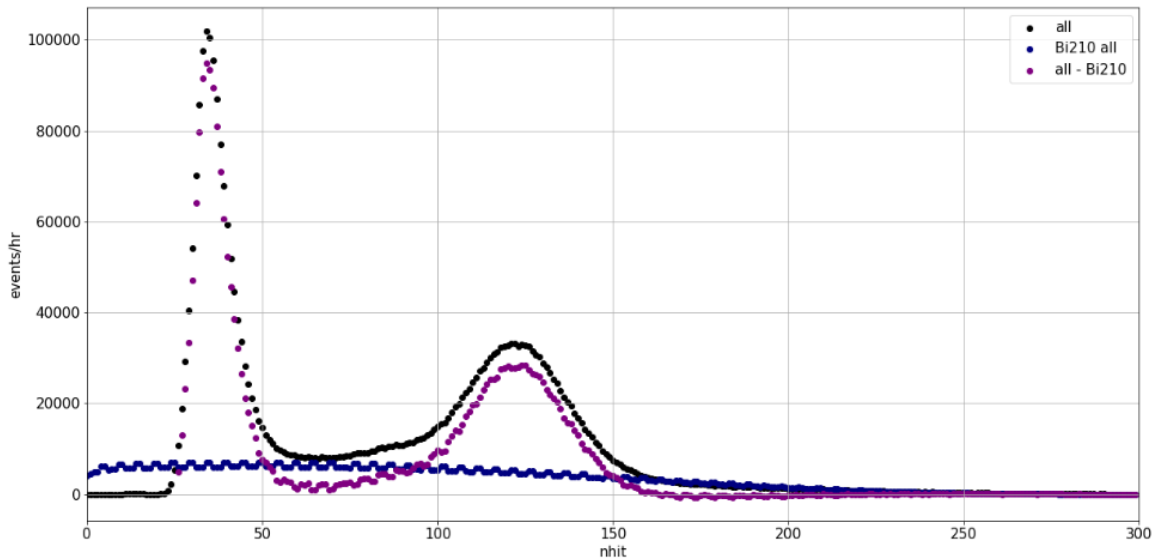
Figure 6.5: Splitting the detector wide nhit spectrum into its major components. The total recorded energy spectrum is in black. The projected energy spectrum of ^{210}Bi is in blue, fit to the total energy spectrum over the range 200 nhits < E < 320 nhits. In purple is the projected ^{210}Po and projected ^{14}C energy spectra derived from subtracting the projected ^{210}Bi energy spectrum from the total energy spectrum

6.3.2 Results: Polonium and Bismuth 210 rates

The application of the aforementioned technique can be extended to multiple consecutive runs, allowing us to observe the temporal evolution of event rates for different decay processes. In Figure 6.6, we present the outcomes of this splitting procedure applied to runs conducted from late April to early May. The plot displays the reconstructed rates of ^{210}Bi (depicted in blue), ^{210}Po (depicted in black), and ^{14}C (depicted in purple) events, as well as the projected ^{210}Bi rate (depicted in green). It is important to note that the reconstructed rates refer to the number of events that have been successfully reconstructed and recorded, satisfying the condition of having an nhit value greater than 25. Conversely, decays with nhit values below 25 are not reconstructed, resulting in a certain proportion of unregistered ^{210}Bi events. The projected ^{210}Bi rate extends the energy spectrum down to 0 nhits, utilizing the smeared energy spectrum and the scaling factors described in Section 6.3.1.

The observed equivalence in event rates between ^{210}Bi and ^{210}Po is in line with expectations based on their respective half-lives and the duration of the experiment. Given that ^{210}Po is produced through the radioactive decay of ^{210}Bi, it is anticipated that over an extended period of time, the event rates of both isotopes would approach a state of equilibrium.
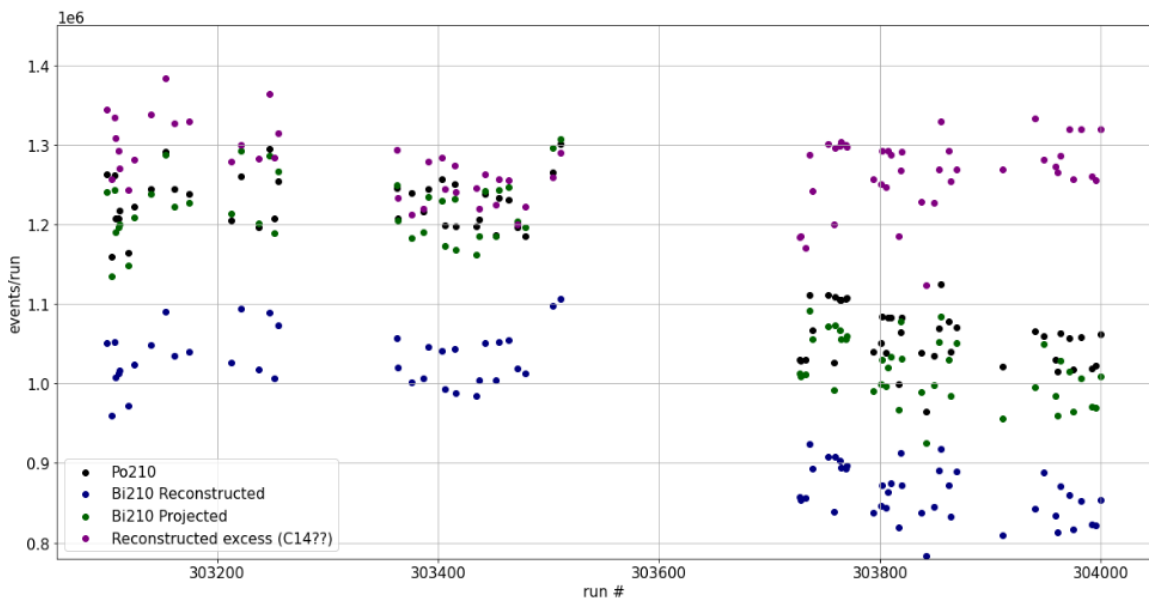
Figure 6.6: ^{210}Po, ^{210}Bi, and excess (^{14}C) rates over time. Equivalence in event rates between ^{210}Bi and ^{210}Po seen as the event rates of both isotopes have reached equilibrium over time.

Chapter 7

Conclusion

The primary objective of this thesis was to comprehensively investigate various aspects of the SNO+ experiment and its associated detector. The thesis was organized into distinct sections, each addressing different elements pertaining to the SNO+ experiment and its backgrounds.

The initial chapter presented an overview of neutrino physics and its historical progression focusing on the aspects most relevant to the SNO+ experiment. Next, an overview of the SNO+ detector was included as a separate chapter to provide a concise understanding of the detector itself.

Following the introductory chapters, the thesis delved into the impact of light reflection on the detector surface. This was undertaken, with a specific emphasis on its influence on event position reconstruction. To address the mis-reconstruction issue, a novel methodology to detect events that were mis-reconstructed was introduced. The implementation of this classifier effectively mitigated mis-reconstruction of events from the detector surface into the detector volume. This mis-reconstruction was eliminated within a radius of 5.1m from the detector center and decreased by a factor of 400 within a radius of 5.5m from the detector center.

The subsequent section of the thesis centered on tracking the origin and flow patterns of unmixed ^{210}Po within the detector. The flow pattern of this material was investigated and an estimate of the volume flow rate of this material given. Further-

more, through the implementation of the mis-reconstruction detection algorithms, it was possible to trace the origin of this material to approximately 10cm from the surface of the detector.

In the final segment of the thesis, attention was devoted to the examination and separation of individual event rates for the major backgrounds present on the detector surface: ^{210}Po, ^{210}Bi, and ^{14}C. A approach was employed involving the theoretical simulation of the energy spectrum of ^{210}Bi. This simulated spectrum was subsequently smeared with Gaussian uncertainty to better align with the observed energy spectrum within the detector. By segregating and analyzing this spectrum from the ^{210}Po and ^{14}C spectra, the thesis successfully determined the separate event rates for each isotope. Notably, this analysis revealed equivalent rates of ^{210}Po and ^{210}Bi, which aligns with their parent-daughter relationship.

The exploration conducted throughout this thesis yields valuable insights into various processes within the SNO+ detector. The detection and mitigation of mis-reconstruction through the classifier, the tracking of unmixed ^{210}Po to a vicinity of approximately 10cm from the detector surface, and the determination of individual event rates for different isotopes on the detector surface collectively contribute to an enhanced understanding of the SNO+ experiment.

Bibliography

[1] S. M. Bilenky, "Neutrino. history of a unique particle," *The European Physical Journal H*, vol. 38, no. 3, pp. 354–404, 2012.

[2] N. G. Tyson, "Little neutral ones," 2023. [Online]. Available: https://www.naturalhistorymag.com/universe/211418/little-neutral-ones.

[3] National Research Council, "Nuclear physics: The core of matter, the fuel of stars," *National Academics Press*, 1999.

[4] C. L. Cowan, Jr., F. Reines, F. B. Harrison, H. W. Kruse, and A. D. McGuire, "Detection of the free neutrino: A confirmation," *Science 124 103–104*, 1956.

[5] Q. R. Ahmad et al . (SNO Collaboration), "Direct evidence for neutrino flavor transformation from neutral current interactions in the sudbury neutrino observatory," *PHYSICAL REVIEW LETTERS*, vol. 89, no. 1, 2002.

[6] Y. Fukuda et al, "Evidence for oscillation of atmospheric neutrinos," *Phys. Rev. Lett*, vol. 81, no. 1562, 1998.

[7] Brookhaven National Laboratory, "Discovery of the muon neutrino," [Online]. Available: https://www.bnl.gov/bnlweb/history/nobel/.

[8] K. Kodama et al, "A first measurement of the interaction cross section of the tau neutrino," 2007. [Online]. Available: https://www.osti.gov/biblio/921523.

[9] Pablo F. de Salas, Stefano Gariazzo, Olga Mena*, Christoph A. Ternes and Mariam Tórtola, "Neutrino mass ordering from oscillations and beyond: 2018 status and future prospects," *Frontiers in Astronomy and Space Sciences*, 2018. DOI: 10.3389/fspas.2018.00036.

[10] B. Aharmim et al. (SNO Collaboration), "Combined analysis of all three phases of solar neutrino data from the sudbury neutrino observatory," *Phys. Rev. C*, vol. 88, no. 025501, 2013.

[11] Manfred Lindner, Tommy Ohlsson, and Gerhart Seidl, "See-saw mechanisms for dirac and majorana neutrino masses," *Phys. Rev. D*, vol. 65, no. 053014, 2002.

[12] Giovanni Benato, "Effective majorana mass and neutrinoless double beta decay," *The European Physical Journal C*, vol. 75, no. 563, 2015.

[13] P. A. R. Ade et al. (Planck Collaboration), "Planck 2015 results," *Astronomy Astrophysics*, vol. 594, no. 13, 2016.

[14] N. P. Delabrouille et al, "Constraint on neutrino masses from sdss-iii/boss ly forest and other cosmological probes," DOI: https://doi.org/10.1088/1475-7516/2015/02/045.

[15] S. Dell'Oro, S. Marcocci, M. Viel, and F. Vissani, "The contribution of light majorana neutrinos to neutrinoless double beta decay and cosmology," *Journal of Cosmology and Astroparticle Physics*, 2015.

[16] Ruben Saakyan, "Two-neutrino double-beta decay," *Annual Review of Nuclear and Particle Science*, vol. 63, pp. 503–529, 2013.

[17] The NEMO experiment, "The two neutrino double beta decay," [Online]. Available: http://nemo.in2p3.fr/physics/dbd.php.

[18] Frank T. Avignone III and Steven R. Elliott, "The search for double beta decay with germanium detectors: Past, present, and future," *Front. Phys*, vol. 7, 2019.

[19] Benjamin J.P. Jones, "The physics of neutrinoless double beta decay: A primer," 2021. arXiv: 2108.09364.

[20] Michelle J. Dolinski, Alan W.P. Poon, and Werner Rodejohann, "Neutrinoless double-beta decay: Status and prospects," *Annual Review of Nuclear and Particle Science*, vol. 69, 2019.

[21] Tereza Kroupová, "Improving the sensitivity to neutrinoless double beta decay in sno+," *Doctoral Thesis, Wolfson College University of Oxford*,

[22] V. Albanese etal. (SNO+ Collaboration), "The sno+ experiment," *JINST*, 2021.

[23] Inácio, A. S., "Data analysis of the water and scintillator phases of sno+ : From solar neutrino measurements to double beta decay sensitivity studies," *Doctoral Thesis, Universidade de Lisboa*, DOI: http://hdl.handle.net/10451/57802.

[24] M. Anderson et al. (The SNO+ Collaboration), "Search for invisible modes of nucleon decay in water with the sno+ detector," *Phys. Rev. D*, vol. 99, no. 032008, 2019.

[25] M. Anderson et al. (SNO + Collaboration), "Measurement of the 8b solar neutrino flux in sno+ with very low backgrounds," *Phys. Rev. D*, vol. 99, no. 012012, 2019.

[26] M. R. Anderson et al. (SNO+ Collaboration), "Development, characterisation, and deployment of the sno+ liquid scintillator," *JINST 16, p.P05009*, 2021.

[27] V. Lozza and J. Petzoldt, "Cosmogenic activation of a natural tellurium target," *Astropart. Phys.*, vol. 61, pp. 62–72, 2015.

[28] Keith R Rielage, [Online]. Available: https://www.researchgate.net/figure/The-222-Rn-decay-chain-The-rare-branches-to-218-At-and-210-Tl-are-removed-for-clarity_fig1_48176556.

[29] P. Khaghani, "Neck sense rope system and leaching studies for sno+," *Masters Thesis, Laurentian Univeristy*, 2016.

[30] "Geant4 developments and applications," *IEEE Transactions on Nuclear Science*, vol. 53, no. 1, pp. 270–278, 2006.

[31]   S. Seibert et al., "Rat (is an analysis tool) user's guide," [Online]. Available: https://rat.readthedocs.io/en/latest/index.html.

[32]   Will Parker, "Multipdf method for position reconstruction," 2021.

[33]   National Nuclear Data Center (NNDC) at Brookhaven National Laboratory, [Online]. Available: https://www.nndc.bnl.gov/nudat3/.

[34]   Thomas Joseph Corona, "Simulation tools for the 2km detector at the t2k experiment," 2023.

[35]   gzangakis, "Beta-spectrum," [Online]. Available: https://github.com/gzangakis/beta-spectrum/blob/master/BetaDecay.py.